catalysts

MDPI

Article

Development of Photocatalytic Coatings for Building Materials with Bi_2O_3-ZnO Nanoparticles

Víctor M. Tena-Santafé [1], José M. Fernández [1], Claudio Fernández-Acevedo [2], Tamara Oroz-Mateo [2], Íñigo Navarro-Blasco [1] and José I. Álvarez [1,*]

[1] MATCH Group, Department of Chemistry, University of Navarra, 31008 Pamplona, Navarra, Spain; victortena.tena@gmail.com (V.M.T.-S.); jmfdez@unav.es (J.M.F.); inavarro@unav.es (Í.N.-B.)
[2] LUREDERRA Technological Centre, 31008 Los Arcos, Navarra, Spain; tamara.oroz@lurederra.es (T.O.-M.)
* Correspondence: jalvarez@unav.es

Abstract: The aim of this study was to develop versatile coatings that can protect the stone surfaces of Architectural Heritage. Two different 3D media, namely superhydrophobic (SPHB) and hydro-oleophobic (OHB), were utilized as host matrices for nanostructured photocatalysts (Bi_2O_3-ZnO 8/92). These photocatalysts were sensitive to visible light to enhance their efficiency when exposed to sunlight. To prevent the nanophotocatalyst from clumping together in the 3D media, non-ionic dispersant additives (Tween20, TritonX-100, and Brij35) were incorporated. The optimized suspensions were then applied to various substrates such as sandstone, limestone, and granite. The effectiveness of the coatings was assessed by evaluating the hydrophobicity, oleophobicity, and photocatalytic activity of the coated substrates. The Bi_2O_3-ZnO photocatalyst exhibited higher activity in the SPHB medium compared to the OHB medium. To simulate real-life conditions, the coated substrates were subjected to accelerated weathering tests to predict their durability. Despite a significant reduction in their thickness, the coatings demonstrated sustained hydrophobic efficiency and self-cleaning capability after the accelerated ageing tests.

Keywords: built heritage; coating; granite; sandstone; limestone; photocatalyst; waterproofing; self-cleaning

Citation: Tena-Santafé, V.M.; Fernández, J.M.; Fernández-Acevedo, C.; Oroz-Mateo, T.; Navarro-Blasco, Í.; Álvarez, J.I. Development of Photocatalytic Coatings for Building Materials with Bi_2O_3-ZnO Nanoparticles. *Catalysts* **2023**, *13*, 1412. https://doi.org/10.3390/catal13111412

Academic Editors: Adrián Pastor Espejo and Luis Sánchez Granados

Received: 10 October 2023
Revised: 31 October 2023
Accepted: 1 November 2023
Published: 3 November 2023

1. Introduction

Artistic, historical, and cultural heritage are vulnerable to numerous factors that contribute to their deterioration. Some notable environmental issues include the accumulation of carbon particles leading to surface blackening, the impact of water, the effects of specific atmospheric gases such as NO_x and COVs, and the growth of microorganisms like fungi and bacteria [1–4]. The infiltration of water through cracks and holes [5,6] can result in the dissolution of salts, the occurrence of efflorescence, and material breakage due to freeze–thaw cycles. Additionally, anthropogenic factors such as pollution and graffiti [7,8] contribute to the deterioration of buildings. Addressing all these concerns demands significant effort and substantial investments. Consequently, numerous treatments have been suggested to mitigate or, at the very least, minimize the damages.

The common approach has been to use waterproofing agents to protect materials from water damage [9–11]. These agents typically consisted of organic compounds like resins, acrylates, and waxes [9,11–15]. In the case of anti-graffiti treatments, various methods have been proposed [16] that allow for the easy removal of graffiti by subjecting the surface material to different cleaning processes. However, these "traditional" treatments, in addition to being short-lived, present several issues, as highlighted by [17]: (1) they cause changes in colour and gloss, resulting in thick coloured coatings [18]; (2) they rely on organic compounds that are incompatible with ancient construction materials and can even be toxic [19]; (3) they excessively and inadequately reduce water vapor permeability,

causing moisture to accumulate within the material [20]. Innovative approaches have been proposed to confront these problems. One such approach involves creating "smart" surfaces by applying photocatalytic compounds that exhibit biocidal activity and reduction in biological growth, as well as dirt degradation ability. These photocatalysts can break the bonds formed between microorganisms and substrates as well as to react with dirt deposits causing their removal [21–25].

The general action mechanism of these catalysts involves utilizing light to create radical species that, through chemical oxidation, break down contaminants and eliminate them. The resulting decomposition product is carried away by moisture or rainfall [26]. The photocatalytic properties of TiO_2 in removing dirt are well-known, and its use offers several advantages, such as low toxicity, high compatibility with construction materials, and superior catalytic activity compared with other metal oxides [26–28]. However, it faces several challenges, including cost, a limited ability to absorb non-ultraviolet visible sunlight [26,27,29], and its primary use in bulk applications rather than coatings (resulting in the waste of photocatalyst within the internal mass of the construction material or limiting its application to new structures, thereby reducing its potential to transform existing structures into decontaminating areas). Given these factors, which significantly reduce its efficiency, two possible solutions arise: (1) modifying the catalyst to enhance its sensitivity towards the visible part of the spectrum [30–33], and (2) utilizing dispersing agents compatible with the studied material to achieve a proper distribution of the catalyst on the surface [34]. In this regard, previous works provided evidence of improvements achieved when TiO_2 was combined with ZnO [35,36]: the presence of ZnO enhanced photostability, increased the lifetime of both electrons and photogenerated holes, and improved the ability to absorb photons at longer wavelengths compared to bare TiO_2. Bismuth oxides have also been explored with this aim due to their availability, low cost, low toxicity, good biocompatibility, and potential for doping and forming cocatalysts [37,38]. Bi_2O_3 has been safely tested for use in dental cements, without manifestations of toxicity [39].

Considering the aforementioned circumstances, the aim of the current work is to investigate the effectiveness of a multifunctional coating comprising both bismuth- and zinc oxide-based photocatalysts (Bi_2O_3-ZnO) along with two types of media: one possessing superhydrophobic properties (SPHB) and the other exhibiting super-hydro-oleophobic characteristics (OHB). The objective is to achieve a synergistic effect where the medium minimizes dirt adsorption while the photocatalyst degrades any adsorbed substance. These media can also provide protection to the catalyst against rainwater wash-off [40], as claimed in previous studies [22,23,40–48]. Contrary to the common use of TiO_2 and organic water-repellent agents as coatings in Built Heritage, the novelty attained in the current study relies on the particular photocatalyst employed as well as on the two specifically functionalized media. Thus, in this research, the SPHB and OHB matrices will consist of three-dimensional (3D) structures of inorganic ceramic nano-oxides that incorporate photocatallytically active nanoparticles. This composition should prove compatible with the inorganic substrates of the heritage materials to be protected. Ensuring the safety of Architectural Heritage materials is crucial. Previous studies have demonstrated the effectiveness of using these coatings in minimizing water and contaminant exposure, which are known to be destructive agents for these materials [34,35,41,42]. The 3D structure is formed by assembling one-dimensional (1D) nanomaterials into higher-order superstructures such as networks, nanoforests, and nanoarrays [49,50]. These materials possess small cavities that allow breathability, preventing the accumulation of water vapor and ensuring a non-sealing form of protection. The photocatalytic active nanoparticles to be studied are heterostructures of Bi_2O_3-ZnO, which are expected to exhibit great activity when exposed to UV-VIS radiation [51–57]. In order to modify the characteristics of the coatings and prevent the anticipated nanoparticle agglomeration, dispersing agents such as Brij35, TritonX-100, and Tween20 were employed. Although anionic dispersing agents have been reported for optimizing coatings [34,58], the three non-ionic mentioned dispersants were, in this case, selected due to the non-polar nature of the solvents to be used (SPHB and OHB) as well as to their strong detergent and

emulsifying capabilities. Finally, three typical Architectural Heritage materials, such as limestone, sandstone, and granite, were tested as recipients for the assayed dispersions applied as coatings.

2. Results and Discussion

2.1. Characterization of the Photocatalytic Nanoparticles

The specific surface area of the Bi_2O_3-ZnO 8/92 nanoparticles was 30.62 ± 0.05 m^2 g^{-1} (Figure 1), and the average size was calculated to be 33 nm, which is in good agreement with those typically obtained by FSP [59]. The percentage of each oxide, as determined by X-ray Fluorescence, was 8.36% for Bi_2O_3 and 90.83% for ZnO, yielding a purity of 99.19% for the synthesized Bi-Zn nanoparticles. Hereinafter, the term "BiZn" will be used to refer to the Bi_2O_3-ZnO (8 wt%/92 wt%) catalyst. The accuracy and purity of the synthesis path of nanoparticles are of great relevance as they guarantee the absence of elements that could potentially distort the photocatalysis measurements and/or hinder the mixing in the carrier media.

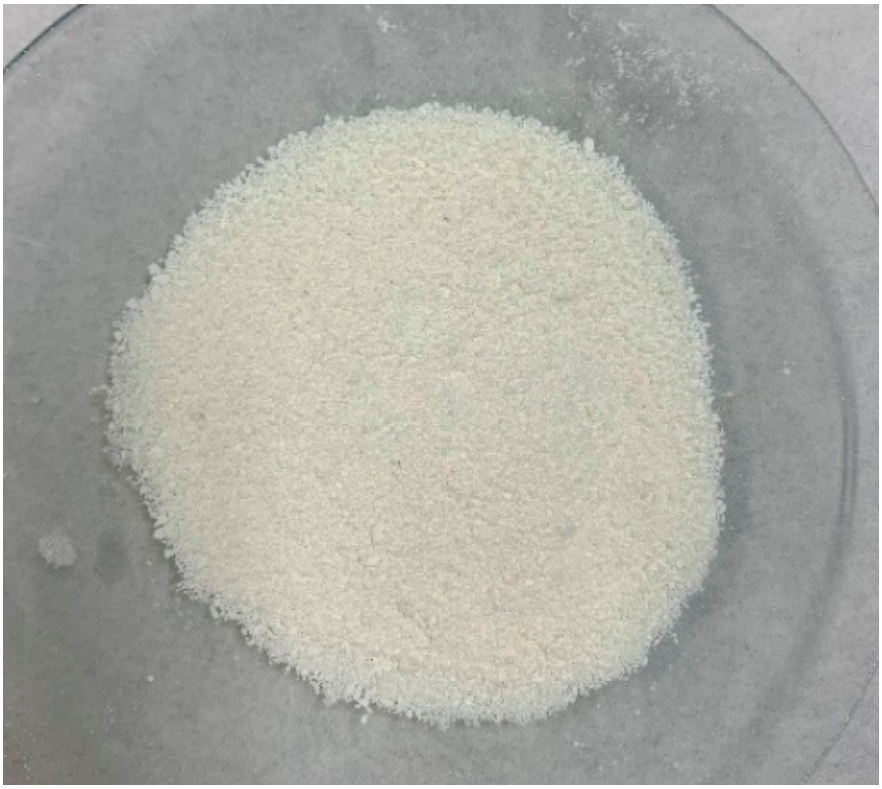

Figure 1. Bi_2O_3-ZnO powder nanoparticles.

Figure 2 illustrates the powdered catalyst's remarkable efficacy in eliminating nitrogen oxides, achieving rates up to 70% when exposed to solar light. These values are scarcely affected (less than 7%) in the absence of UV radiation, clearly proving the notable ability of BiZn nanoparticles to bring down NO levels without generating an excessive amount of the toxic intermediate, NO_2. The selectivity values (S = NO_x removal rate/NO removal rate), which inform the ratio of degraded NO that is converted into non-toxic nitrate rather than forming NO_2, were as high as 95.5% under solar light illumination and even higher (95.8%) for the nanoparticles subjected to just visible light irradiation. The results for Bi_2O_3-ZnO heterostructures showed better NO and NO_x degradation performances under both sunlight and visible light compared with TiO_2-ZnO (50:50) and (10:90) heterostructures [35].

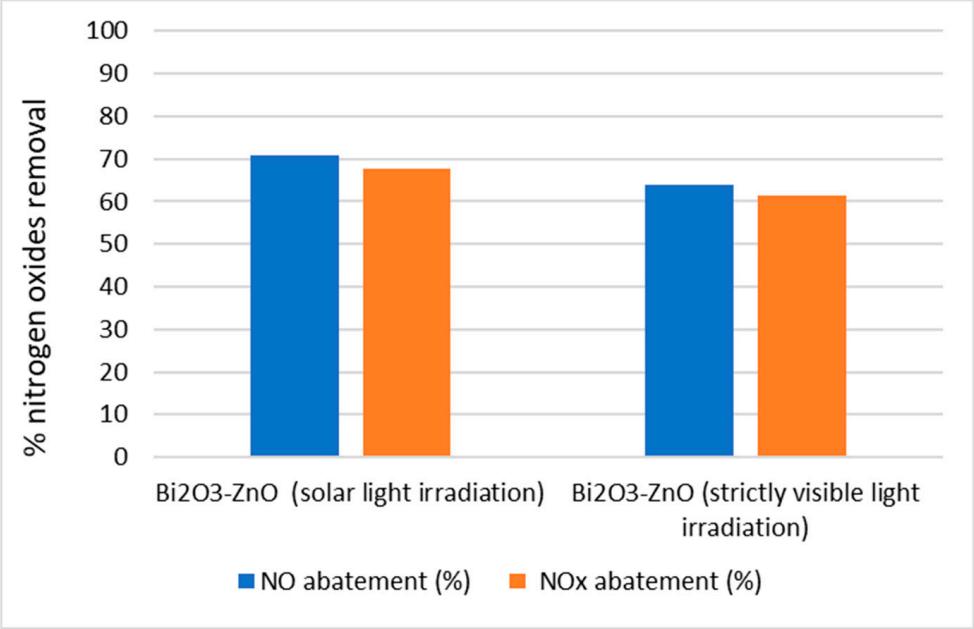

Figure 2. NO and NO_x removal capacity of the powdered nanoparticles of the photocatalyst under solar and visible light irradiation.

2.2. Influence of the Non-Ionic Dispersing Agents on the Distribution of the Photocatalytic Nanoparticles

Zeta potential titration curves can be seen in Figure 3, which show that as the amount of plasticizer increases, the zeta potential acquires more negative values. In line with the electrical double-layer model, the outer surface surrounding nanoparticles comprises two ionic layers, and their electrical charge can be quantified as the zeta potential [60]. This zeta potential serves as an indicator of the extent of repulsion between neighbouring charged particles within a dispersion. When the zeta potential exhibits high absolute values, it signifies that the particles are electrically stabilized, preventing the formation of flocs [61]. Therefore, it can be inferred that the dispersing agents employed obstruct particle–particle interactions by establishing interactions between particles and the dispersant, thereby enhancing the system's stability. The comparison of results also demonstrates superior outcomes for SPHB (zeta potential values below −45 mV in all instances at the end of the titration). The decrease in the zeta potential values of the non-ionic polymers might be ascribed to the greater effective volume of the photocatalytic nanoparticles as a consequence of the adsorption of the polymer, resulting in thicker layers [62].

In general, there are no notable distinctions between the dispersants, and this can be attributed to their comparable Hydrophilic–Lipophilic Balance (HLB) values: 16.7 for Tween20, 13.5 for TritonX-100, and 16.9 for Brij35. However, the lesser decrease in the zeta potential in the SPHB medium with Brij 35 could be ascribed to its lower molecular weight (230.39 g mol^{-1}) as compared with the MW of Tween 20 (522.7 g mol^{-1}) and Triton X-100 (625 g mol^{-1}).

Results show that the dispersing agents tend to stabilize the system by electrostatic repulsions between nanoparticles. However, the concentration of the dispersing agent has been reported to exert a strong influence [63–65]. Zeta potential values, in Table 1, follow two different patterns depending on which dispersant is being used (see in Section 3.2.2 below the detailed composition of each one of the dispersions). Thus, in the OHB medium, the larger the percentage of dispersant, the more stabilizing negative values are obtained, whereas, in the SPHB medium, the absolute zeta potential values were lower for higher ratios of the non-ionic surfactants.

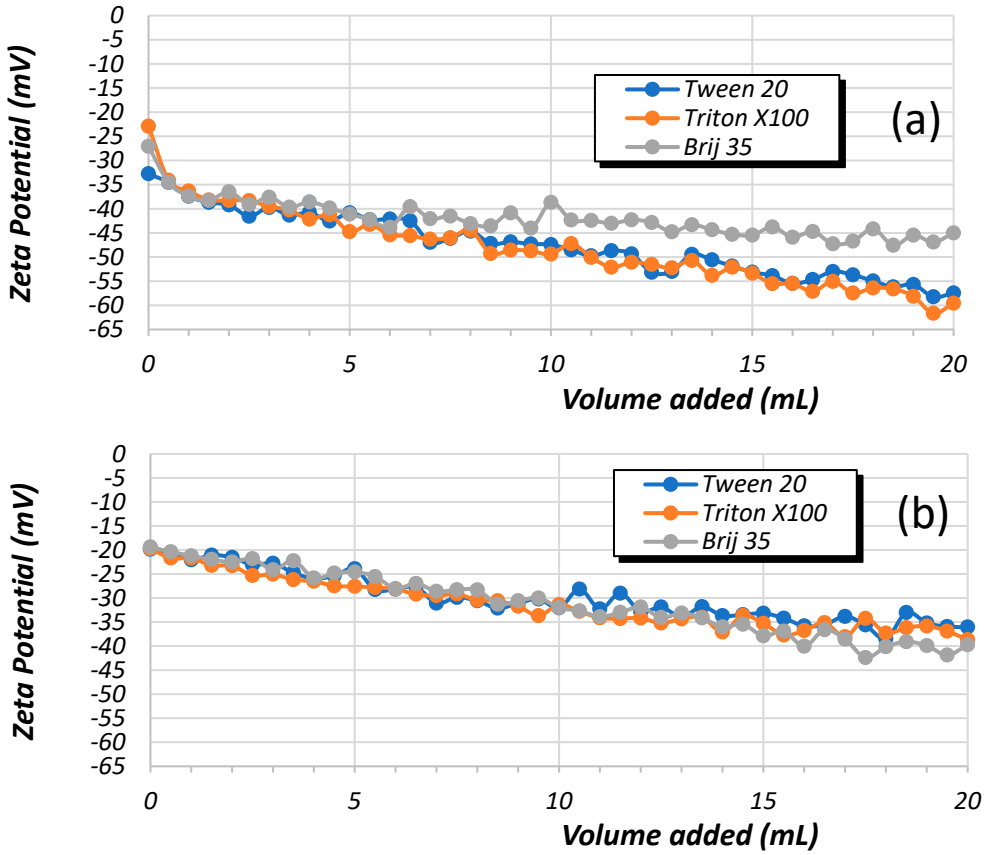

Figure 3. Zeta potential titration of a colloidal suspension of BiZn nanoparticles with dispersing agents used as titrants. (**a**) BiZn in SPHB. (**b**) BiZn in OHB.

Table 1. Net values of zeta potential of dispersion of BiZn in SPHB and OHB media.

SPHB		OHB	
Dispersions	**Average (mV)**	**Dispersions**	**Average (mV)**
BiZn1	−24.91 ± 1.22	BiZn8	−28.70 ± 0.87
BiZn2	−30.42 ± 0.91	BiZn9	−44.30 ± 0.87
BiZn3	−35.52 ± 1.45	BiZn10	−40.40 ± 1.52
BiZn4	−31.37 ± 1.42	BiZn11	−38.00 ± 0.49
BiZn5	−34.73 ± 1.39	BiZn12	−38.90 ± 0.41
BiZn6	−35.32 ± 2.11	BiZn13	−34.70 ± 1.36
BiZn7	−24.94 ± 1.01	BiZn14	−32.80 ± 0.41

In the SPHB medium, the zeta potential values suggested the strongest repulsion for Tween 20 (3%, sample BiZn3), which was later confirmed by the particle size distribution measurements carried out by laser diffraction (Figure 4). As compared with the dispersant-free colloidal system, the presence of the tested surfactants reduced agglomeration, shifting the peak of the maximum particle population towards smaller diameters.

The same correlation between the zeta potential values and the effectiveness as a dispersing agent was observed in the OHB medium. Results in Figure 4 showed that the sample BiZn9, with the most negative zeta potential value, was the one with the lowest average diameter of the predominant particle population.

In both matrices, employing Brij-35 at its highest concentration (3%) led to a displacement of the main peak in particle size diameter towards smaller values, even though the zeta potential absolute values were relatively low. The capacity of this surfactant to maintain stability in the colloidal dispersions is attributed to its steric hindrance effect.

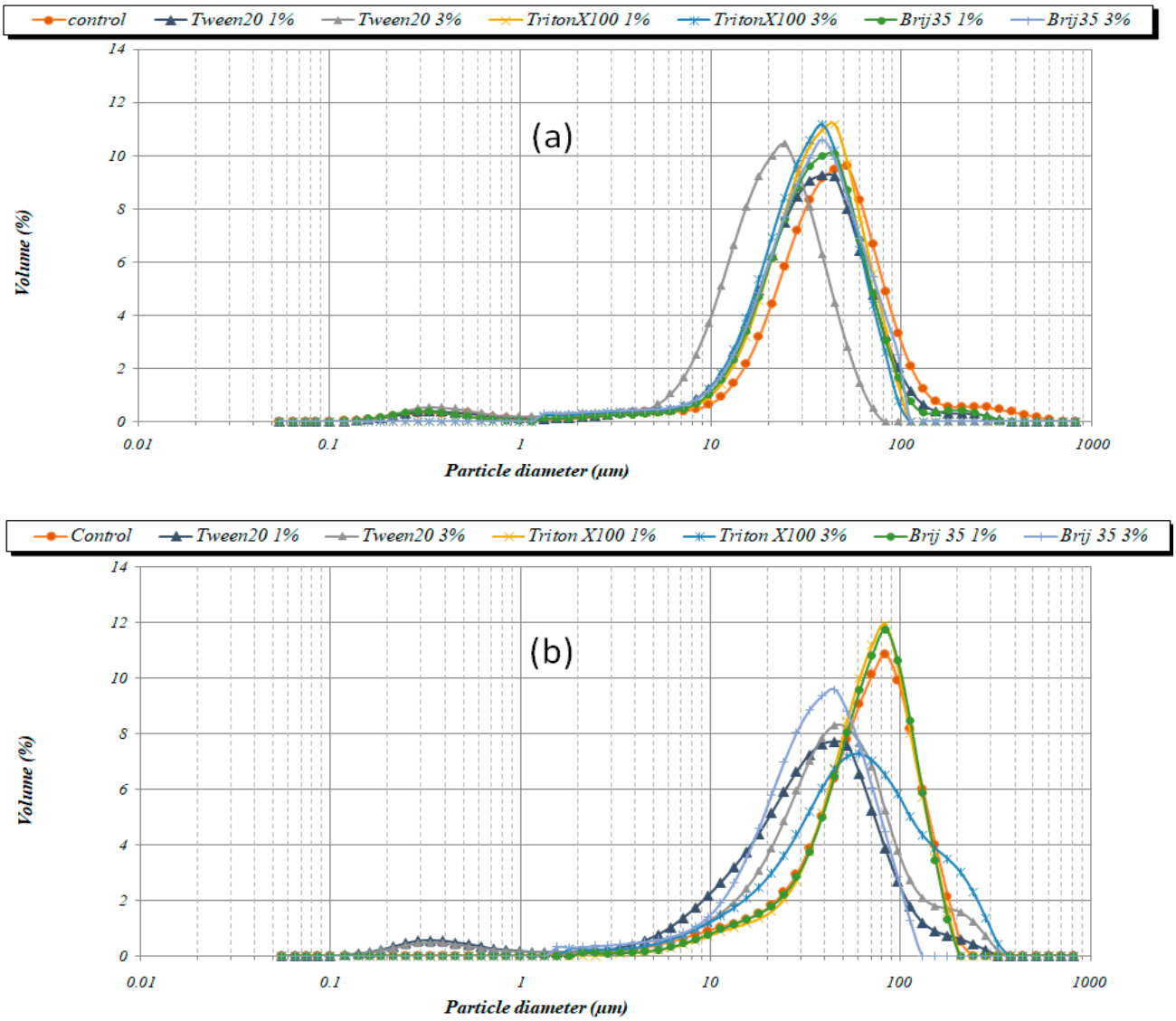

Figure 4. Particle size distribution of the BiZn dispersions in (**a**) SPHB, (**b**) OHB.

The absence of a clear dose–response pattern as a function of the percentage of surfactant can be explained as follows: when the concentration surpasses a certain threshold, the dispersant concentration becomes sufficiently elevated to enable interactions between dispersant molecules, thereby promoting agglomeration.

2.3. Characterization of the Coatings

Every designed coating was applied onto the three intended supports, and the thicknesses of all of them are depicted in Table 2.

As it can be observed, all available data are within the 30–50 microns range, which indicates that neither medium (SPHB or OHB) nor the dispersants (Tween20, TritonX-100, or Brij35) have a marked effect on the thickness of coatings [63–65]. In general, the thickness follows the sandstone > limestone > granite trend, which can be attributed to the roughness [35]. The rougher the surface, the greater the surface–catalyst friction. The logical increase in the superficial area in the substrates with the highest roughness implies a better bonding for the catalyst [66].

The water and hexadecane contact angle values are plotted in Figure 5. Generally, the higher the dispersant percentage, the higher the static contact angle's values. This can be attributed to the dispersant's propensity to facilitate the production of smaller particles,

leading to a more even distribution across the surface and ensuring more uniform coatings, avoiding agglomerations of nanoparticles in which the hydrogen bonds might take place with the water drop.

Table 2. Thickness values of the coatings with BiZn nanoparticles.

SPHB		OHB	
Dispersions	**Results (Microns)**	**Dispersions**	**Results (Microns)**
BiZn1 granite	31.00 ± 0.00	BiZn8 granite	37.00 ± 0.00
BiZn1 limestone	38.50 ± 0.71	BiZn8 limestone	34.00 ± 2.83
BiZn1 sandstone	38.00 ± 1.41	BiZn8 sandstone	34.00 ± 1.41
BiZn2 granite	31.00 ± 0.00	BiZn9 granite	37.50 ± 0.71
BiZn2 limestone	35.50 ± 0.71	BiZn9 limestone	36.00 ± 0.71
BiZn2 sandstone	33.50 ± 0.71	BiZn9 sandstone	34.50 ± 0.71
BiZn3 granite	32.50 ± 0.71	BiZn10 granite	35.50 ± 0.71
BiZn3 limestone	40.50 ± 0.71	BiZn10 limestone	33.50 ± 0.71
BiZn3 sandstone	37.50 ± 0.71	BiZn10 sandstone	35.50 ± 0.71
BiZn4 granite	37.50 ± 0.71	BiZn11 granite	32.50 ± 0.71
BiZn4 limestone	40.00 ± 1.41	BiZn11 limestone	28.50 ± 0.71
BiZn4 sandstone	39.50 ± 2.12	BiZn11 sandstone	47.50 ± 0.71
BiZn5 granite	38.00 ± 1.41	BiZn12 granite	27.50 ± 0.71
BiZn5 limestone	40.00 ± 2.83	BiZn12 limestone	33.50 ± 0.71
BiZn5 sandstone	39.00 ± 2.83	BiZn12 sandstone	34.00 ± 1.41
BiZn6 granite	39.50 ± 2.12	BiZn13 granite	26.50 ± 0.71
BiZn6 limestone	44.50 ± 0.71	BiZn13 limestone	25.00 ± 1.41
BiZn6 sandstone	40.50 ± 0.71	BiZn13 sandstone	34.50 ± 0.71
BiZn7 granite	37.50 ± 0.71	BiZn14 granite	26.50 ± 0.71
BiZn7 limestone	46.50 ± 2.12	BiZn14 limestone	26.50 ± 2.12
BiZn7 sandstone	41.00 ± 1.41	BiZn14 sandstone	45.50 ± 0.71

The static angle exhibits a certain correlation with substrate characteristics, typically ranking as sandstone > limestone > granite. A surface with a higher degree of roughness results in drops settling on the surface's peaks, diminishing the contact area, causing drop deformations, and ultimately, increasing the contact angle.

As for solvents, it is evident that coatings in the SPHB medium exhibit greater hydrophobicity compared with those employing OHB as the hosting matrix. When testing water droplets, certain SPHB coatings can surpass a 150° angle, confirming the exhibition of the lotus effect. This denotes a superhydrophobic system where, despite contact with the surface, the droplet maintains its spherical shape, enabling it to effortlessly roll and remove contaminants from the surface, effectively self-cleaning the surface. Tests conducted with hexadecane as the contacting liquid revealed lower contact angle values than those observed with water. This discrepancy can be attributed to the relatively weaker cohesive forces between the molecules of hexadecane in the droplets (London forces) when compared to the cohesive forces in water (hydrogen bonds). When cohesive forces are strong, adhesive forces to the substrate are diminished, resulting in higher contact angle values, as observed with water.

The current study also checked the photocatalytic effectiveness of the coatings once they were applied to the substrates. Figure 6 displays the abatement results. It is worth emphasizing that the coatings contained only 1% (wt/vol) of the photocatalyst. Therefore, a decrease in NO_x abatement can be anticipated in comparison to the results obtained with the powdered catalyst.

The SPHB coatings were capable of removing, on average, ca. 10% of NO under solar irradiation. Some treated substrates were able to degrade between 10 and 15% and a few samples above 15%. Removal of NO_x yielded lower percentages. According to the norm UNE 127197-1:2013 [67], for catalytic concrete products, the coatings onto limestone would be classified on average as Class 1 (NO_x removal between 4.0 and 6.0%) and the coatings onto sandstone as Class 2 (range of removal 6.0–8.0%). Coatings applied onto

granite were not able to remove NO_x above 4.0% on average, although samples BiZn1 and BiZn7 were able to remove, respectively, 7.0% and 5.7% of NO_x (Class 2 and 1, respectively). Some previous work with pure TiO_2 nanoparticles reported, on average, higher NO and NO_x abatements, but the experimental conditions are not comparable. In particular, the illumination in most of these works was strictly UV [68–70].

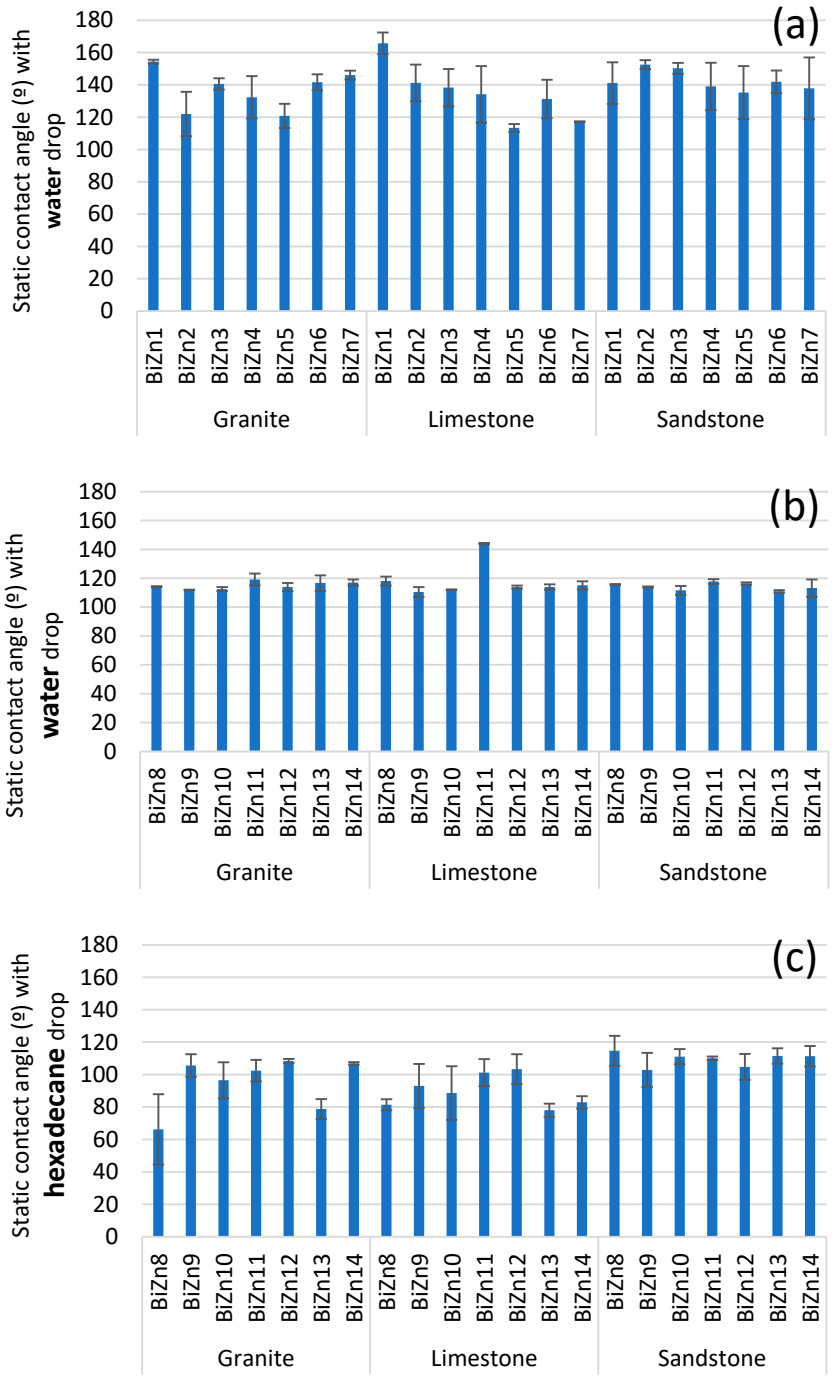

Figure 5. Static contact angle: (**a**) SPHB coatings with water; (**b**) OHB coatings with water; (**c**) OHB coatings with hexadecane.

Under strictly visible irradiation, the NO and NO_x removal values were seen to decrease in comparison with the solar irradiation. This finding had been previously reported in other photocatalytic nanoparticles: the illumination with UV light always provides great efficiency to the photocatalytic oxidation of nitrogen oxides. In this case, ZnO—owing to its

wide band gap—exhibits an absorption peak at a wavelength of 378 nm [71]. In spite of the modification of some parts of the ZnO due to the formation of some heterojunctions with Bi_2O_3 (which was added up to a maximum of 8% wt/wt), the cut-off with the filter of the wavelengths below 410 nm involved a dramatic decrease in the activity of the predominant ZnO. In addition, previous studies have shown that the absorption edges of heterojunctions of Bi_2O_3 and ZnO from 5% to 15% of Bi_2O_3 range between 419 nm and 409 nm, so the filter might also have had a strong influence on the decrease in the visible light activity of these samples.

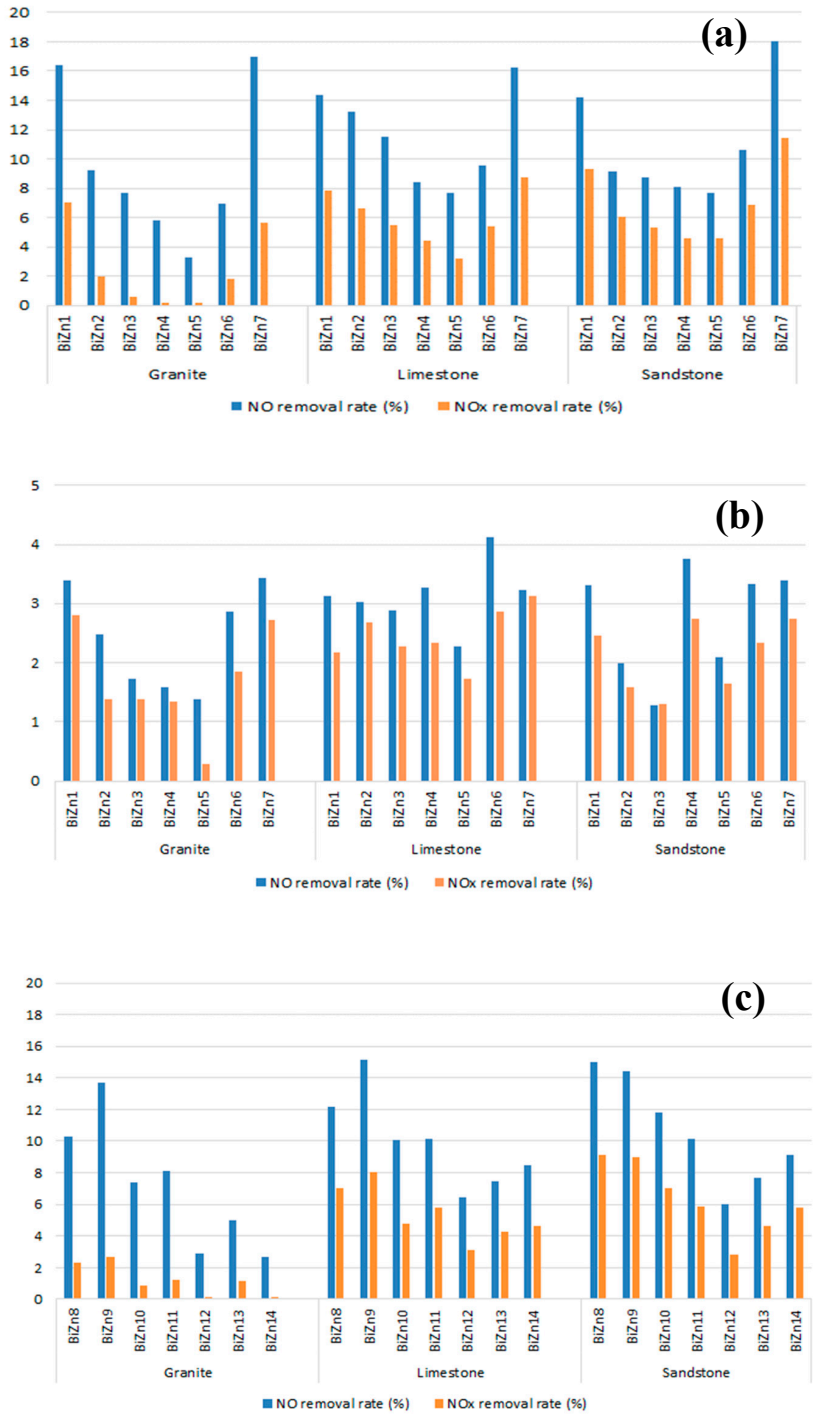

Figure 6. *Cont.*

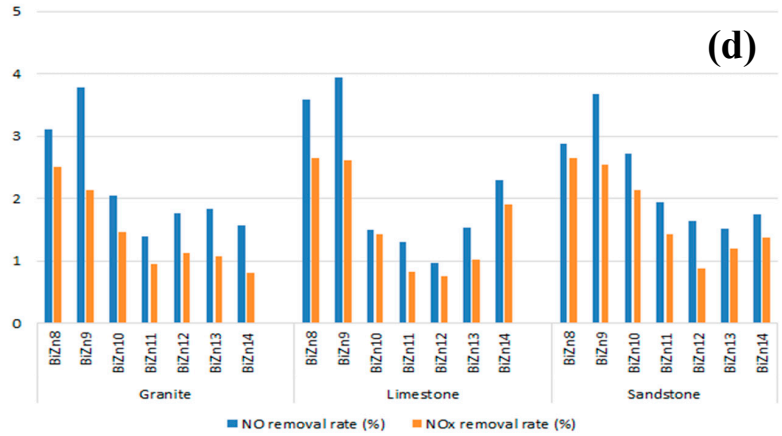

Figure 6. Photocatalytic NO and NO_x removal rates of the SPHB coatings under (**a**) solar and (**b**) visible irradiation, as well as OHB coatings under (**c**) solar and (**d**) visible irradiation.

The noticeable decrease in activity of the coatings with respect to the photocatalyst in the powdered samples (results of Figure 2) has two causes: on the one hand, the low percentage of photocatalyst in the coating, which is only 1% (wt/vol) and, on the other hand, the fact that the active nanoparticles are embedded in the SPHB or OHB matrix, reducing their direct contact with the nitrogen oxides. Here, the more penetrating and energetic UV radiation is also critical to reach and activate nanoparticles that are more shielded by the hydrophobic matrix.

This shielding of the active nanoparticles was even more intense with the hydro-oleophobic matrix, OHB, with a different chemical composition. Also, with solar lighting, the limestone and sandstone substrates could be classified as Class 2 and Class 1 due to their NO_x reduction percentages. On average, the photocatalytic activity under visible illumination was lower than that observed with SPHB matrix coatings. The greater particle size observed in OHB coatings, when compared with SPHB coatings, can also be put forth as a rationale for this observation. In SPHB coatings, it was evident that using Brij35 at the highest dosage proved to be the most efficient dispersing agent for enhancing photocatalytic activity. This observation aligns with the earlier discussed reduction in particle size. On the other hand, in OHB coatings, Tween20 emerged as the most effective dispersant, which is consistent with the particle size distribution measurements.

Regarding the impact of assayed substrates, it is noteworthy that both SPHB and OHB coatings exhibit superior performance on limestone. This is due to the enhanced adsorption of NO and NO_x and their subsequent photocatalytic degradation, facilitated by the substrate's rich composition in alkaline-earth metal oxides and carbonates [72]. The results indicate that granite, as a support, yielded the least effective results in terms of NO and NO_x abatement.

Apart from its chemical composition, the smoother surface of the granite specimen may influence the distribution of the photocatalyst on the stone surface, thereby affecting its photocatalytic effectiveness. Additionally, when used as a support, coatings on granite were the thinnest of all. The lower porosity of granite is also a relevant factor to consider since it limits the penetration of the coating and, accordingly, its activity.

2.4. Durability of the Coatings

All assayed samples comprising the different coatings onto the various substrates were subjected to accelerated climatic ageing to simulate the wear and tear that the coatings would undergo in an actual environmental setting. Table 3 summarizes the percentage of coating thickness that has been lost as a result of wear.

As a result of the simulated climatic ageing, a reduction in thickness was observed, which was more pronounced for OHB coatings compared with SPHB coatings. On average, there was a 15.1% decrease in thickness for OHB coatings, while SPHB coatings experienced

an 11.4% reduction. These findings indicate that a washing and drag-out of the coating material has taken place, along with a leaching phenomenon.

Table 3. Thickness reduction (%) after accelerated climatic ageing.

SPHB		OHB	
Dispersions	**% Loss of Thickness**	**Dispersions**	**% Loss of Thickness**
BiZn1 granite	1.6	BiZn8 granite	20.3
BiZn1 limestone	1.3	BiZn8 limestone	11.8
BiZn1 sandstone	15.8	BiZn8 sandstone	13.2
BiZn2 granite	17.7	BiZn9 granite	22.7
BiZn2 limestone	7.0	BiZn9 limestone	11.1
BiZn2 sandstone	3.0	BiZn9 sandstone	17.4
BiZn3 granite	3.1	BiZn10 granite	15.5
BiZn3 limestone	4.9	BiZn10 limestone	22.4
BiZn3 sandstone	12.0	BiZn10 sandstone	21.1
BiZn4 granite	8.0	BiZn11 granite	16.9
BiZn4 limestone	5.0	BiZn11 limestone	0.0
BiZn4 sandstone	12.7	BiZn11 sandstone	32.6
BiZn5 granite	9.2	BiZn12 granite	3.6
BiZn5 limestone	8.8	BiZn12 limestone	20.9
BiZn5 sandstone	19.2	BiZn12 sandstone	10.3
BiZn6 granite	11.4	BiZn13 granite	3.7
BiZn6 limestone	16.9	BiZn13 limestone	6.0
BiZn6 sandstone	17.3	BiZn13 sandstone	26.1
BiZn7 granite	13.3	BiZn14 granite	0.0
BiZn7 limestone	30.1	BiZn14 limestone	5.7
BiZn7 sandstone	22.0	BiZn14 sandstone	35.2

The contact angle also saw a decrease following the ageing process (Figure 7), particularly in OHB coatings as opposed to SPHB coatings. The hydrophobicity decreased more significantly in the OHB-treated samples. After the degradation due to climatic ageing, all measured water contact angles for SPHB coatings were below 150°, resulting in the loss of superhydrophobicity. However, water repellency was maintained in nearly all samples treated with SPHB coatings, with water contact angles above 90°. This was also true for OHB coatings applied onto sandstone. Oleo-repellency experienced a substantial reduction, confirming the damage caused by accelerated climatic ageing.

The surface wettability assessment method using the dynamic contact angle study ('advance and receding contact angle', ARCA) was also carried out on coatings once they had been subjected to accelerated climatic ageing (Figure 8). This method gives a closer idea of the reality of non-ideal surfaces with chemical and topological heterogeneities.

The advance angle (ACA) primarily pertains to how the surface interacts with the liquid in the test, either attracting or repelling it, and is particularly influenced by the surface's hydrophobic properties. Conversely, the receding angle (RCA) is more associated with the hydrophilic interplay between the liquid (water) and the surface due to adhesion forces.

On an ideal surface that is completely smooth, uniform, and unreactive, the hysteresis (the difference between ACA and RCA) would be zero. Surfaces with high hysteresis values imply situations of significant heterogeneity, including high roughness and/or chemical diversity. On such surfaces, water droplets would exhibit limited mobility. In the instance of superhydrophobic surfaces, both ACA and RCA are anticipated to exceed 150°, and these surfaces are also expected to resist the adhesion of liquid droplets, resulting in low hysteresis values. Hysteresis values obtained after these measurements are presented in Table 4.

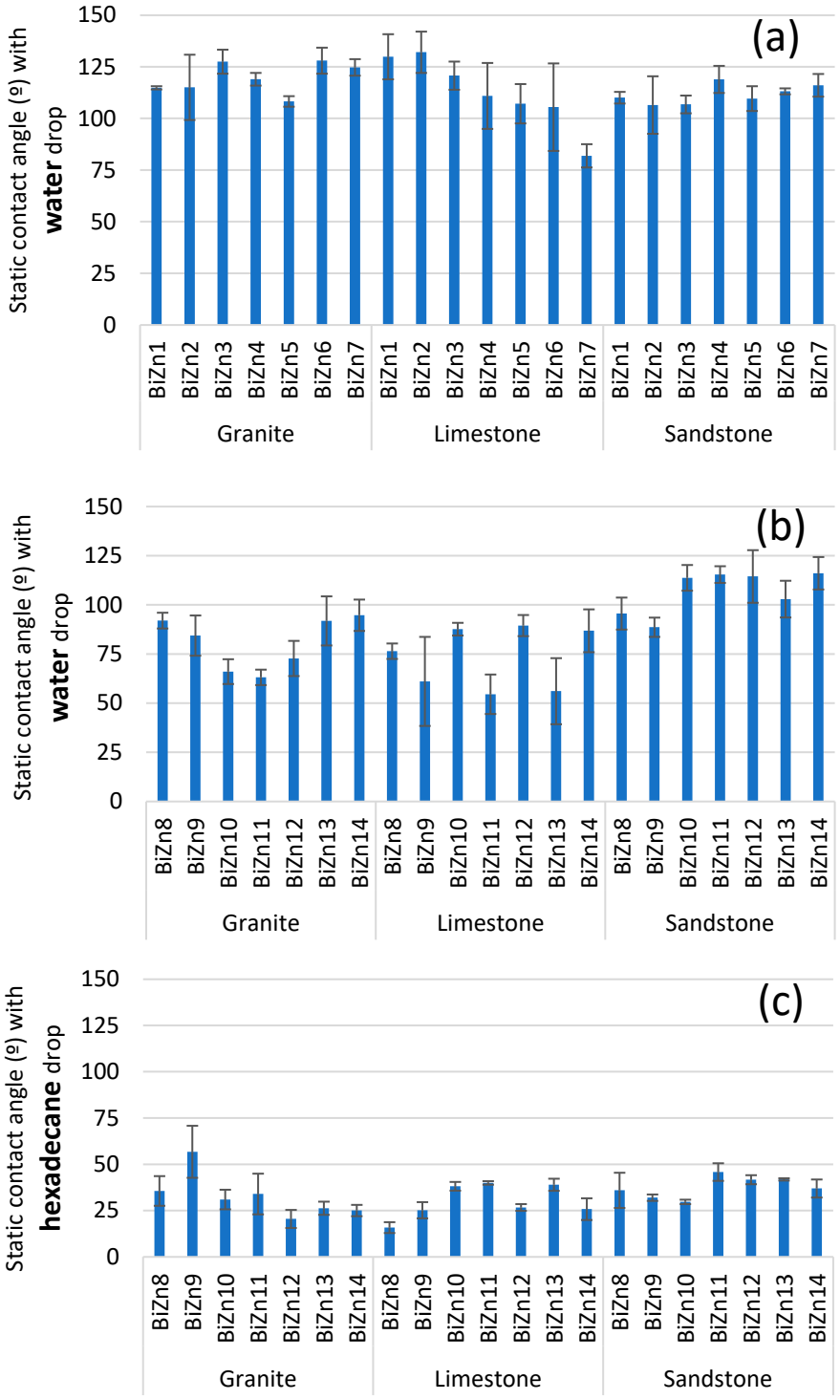

Figure 7. Static contact angle after climatic ageing of (**a**) SPHB coatings with water, (**b**) OHB coatings with water, (**c**) OHB coatings with hexadecane.

These experimental values revealed that superhydrophobicity was no longer present following exposure to climatic ageing. However, in the ARCA dynamic measurements, ACA values were below 150°. It is worth noting, however, that, in some cases, the values came very close to this threshold, indicating that despite the deterioration they underwent, a number of samples still showed a persistent water-repelling effect.

The coatings applied on limestone exhibited the lowest average hysteresis. This suggests that the adhesion of water droplets is expected to be quite minimal. Even after

enduring accelerated weathering, the coating remains effective in safeguarding the material from water penetration. On the other hand, granite and sandstone exhibited higher average hysteresis values. This is due to chemical heterogeneity in the case of granite, resulting in increased interactions between water droplets or hexadecane and the substrate. In the case of sandstone, it is attributed to its topological heterogeneity, namely its rough surface. Limestone, being more homogeneous in composition and less rough, yielded lower hysteresis.

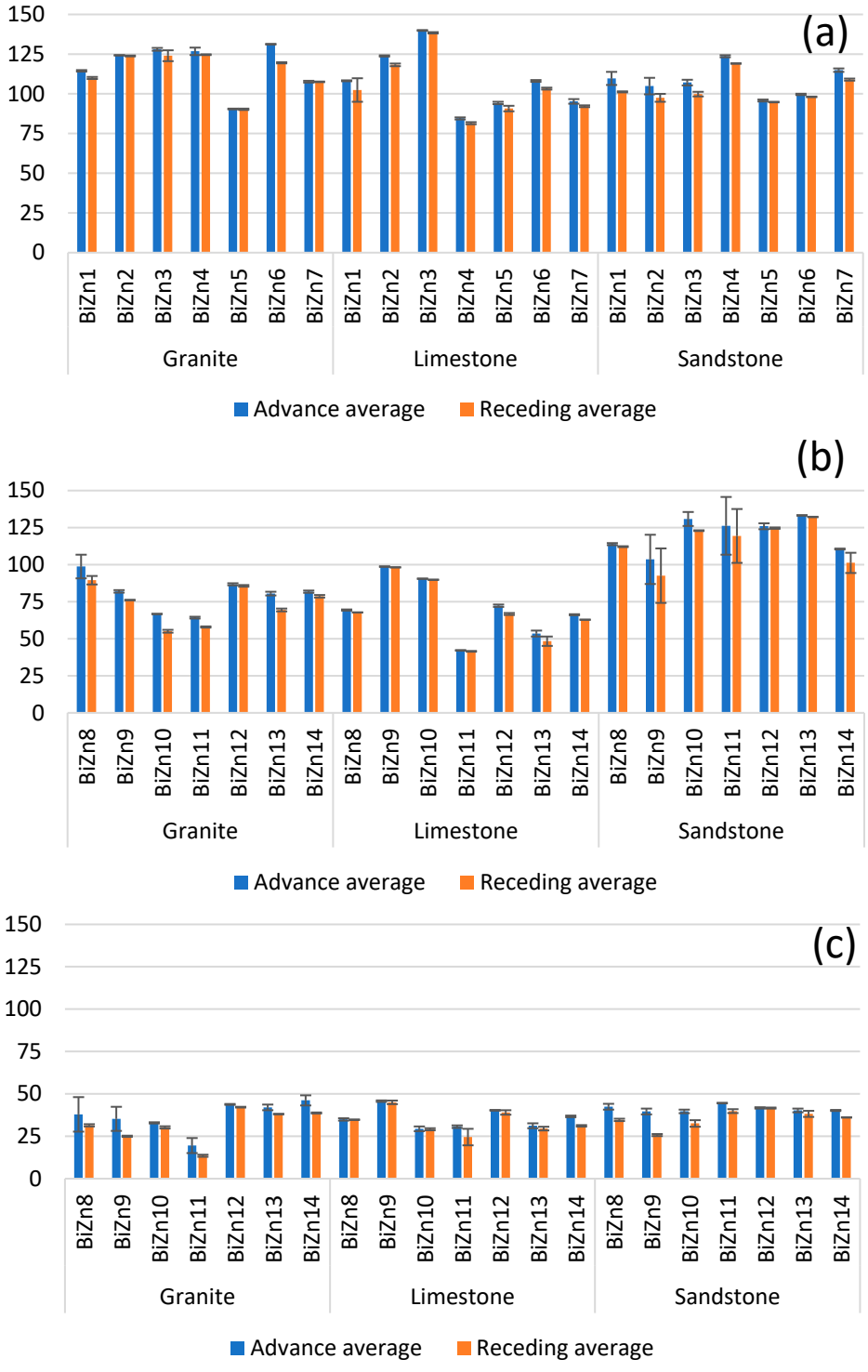

Figure 8. Advance (ACA) and receding (RCA) contact angle after climatic ageing of (**a**) SPHB coatings with water, (**b**) OHB coatings with water, (**c**) OHB coatings with hexadecane.

Considering the positive outcomes regarding the durability of the treated limestone, an AFM analysis was conducted on a sample of this material coated with SPHB (designated as sample BiZn1) both before and after undergoing an ageing process. The aim was to assess any alterations in surface roughness and composition.

Table 4. Hysteresis (difference between ACA and RCA dynamic studies of the contact angle after climatic ageing).

	Hysteresis (Water)		**Hysteresis (Water)**		**Hysteresis (Hexadecane)**
BiZn1 granite	4.47	BiZn8 granite	9.24	BiZn8 granite	6.45
BiZn1 limestone	5.81	BiZn8 limestone	1.58	BiZn8 limestone	0.16
BiZn1 sandstone	8.46	BiZn8 sandstone	1.74	BiZn8 sandstone	7.76
BiZn2 granite	0.42	BiZn9 granite	5.90	BiZn9 granite	10.27
BiZn2 limestone	5.61	BiZn9 limestone	0.52	BiZn9 limestone	0.70
BiZn2 sandstone	7.38	BiZn9 sandstone	11.00	BiZn9 sandstone	13.91
BiZn3 granite	3.96	BiZn10 granite	11.63	BiZn10 granite	2.66
BiZn3 limestone	1.50	BiZn10 limestone	0.68	BiZn10 limestone	0.25
BiZn3 sandstone	7.27	BiZn10 sandstone	7.88	BiZn10 sandstone	7.08
BiZn4 granite	2.15	BiZn11 granite	6.33	BiZn11 granite	6.01
BiZn4 limestone	2.99	BiZn11 limestone	0.69	BiZn11 limestone	6.17
BiZn4 sandstone	4.58	BiZn11 sandstone	6.82	BiZn11 sandstone	4.78
BiZn5 granite	0.15	BiZn12 granite	1.04	BiZn12 granite	1.64
BiZn5 limestone	3.50	BiZn12 limestone	5.59	BiZn12 limestone	1.29
BiZn5 sandstone	0.97	BiZn12 sandstone	1.34	BiZn12 sandstone	0.07
BiZn6 granite	11.69	BiZn13 granite	11.01	BiZn13 granite	3.96
BiZn6 limestone	4.84	BiZn13 limestone	5.14	BiZn13 limestone	1.66
BiZn6 sandstone	1.55	BiZn13 sandstone	1.01	BiZn13 sandstone	1.96
BiZn7 granite	0.10	BiZn14 granite	3.10	BiZn14 granite	7.40
BiZn7 limestone	3.08	BiZn14 limestone	3.37	BiZn14 limestone	5.55
BiZn7 sandstone	5.92	BiZn14 sandstone	9.30	BiZn14 sandstone	4.19

A 10 × 10 micron scan provided insight into the coating's surface (Figure 9). In its original state, the coating exhibited a relatively uniform coverage over the observed region. However, in the modified specimen, a smoother area with fewer irregularities was observed.

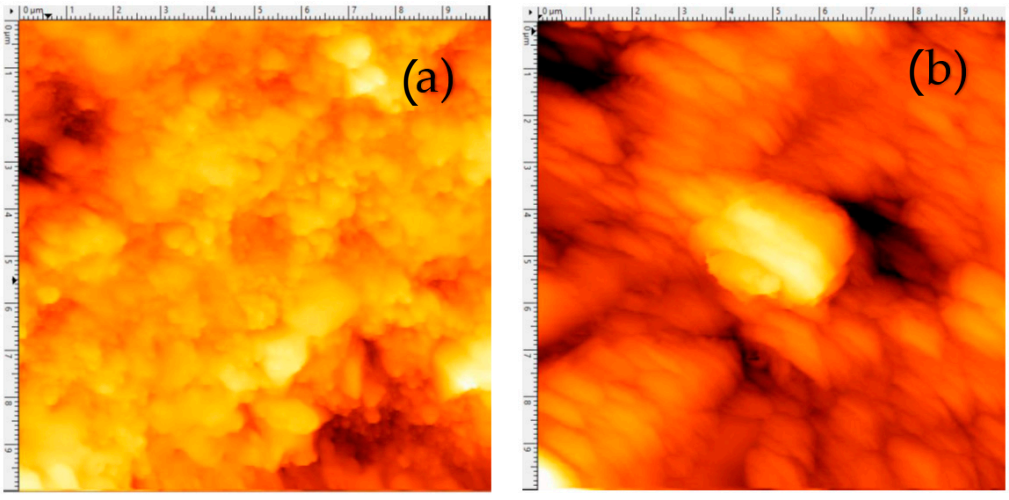

Figure 9. *Cont.*

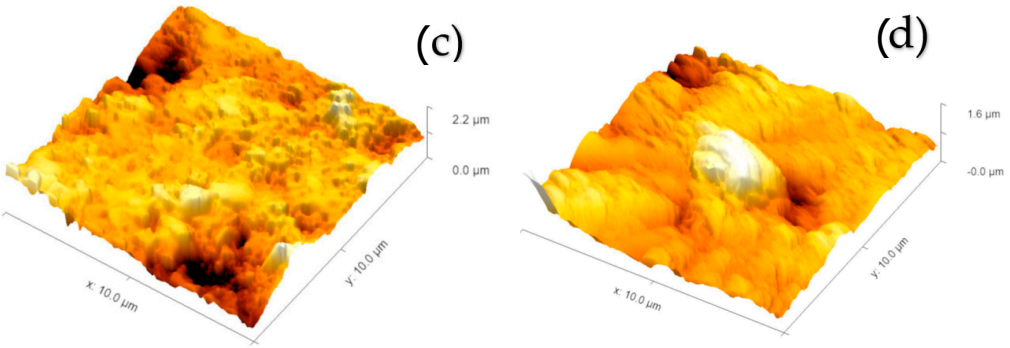

Figure 9. Coating's surface changes as consequence of climate ageing (**a**) before and (**b**) after the ageing. Three-dimensional rendering of surface's coating (**c**) before and (**d**) after ageing.

This phenomenon was also evident in the 3D renderings of the 10 × 10 micron regions (Figure 9). It was observed that the ageing process led to a smoothing of the material's surface and a decrease in its overall height variation.

Upon closer inspection, it became feasible to ascertain the topography of the ceramic nano-oxides that govern the characteristics of the SPHB coating. The textural porosity (Figure 10a,b), facilitating the breathability of the stone substrates onto which the coating is applied, was duly observed. After the accelerated degradation, the surface of the deteriorated coating appears more worn and smoother when compared to the almost step-like pattern exhibited by the original sample topographic scan (Figure 10c,d).

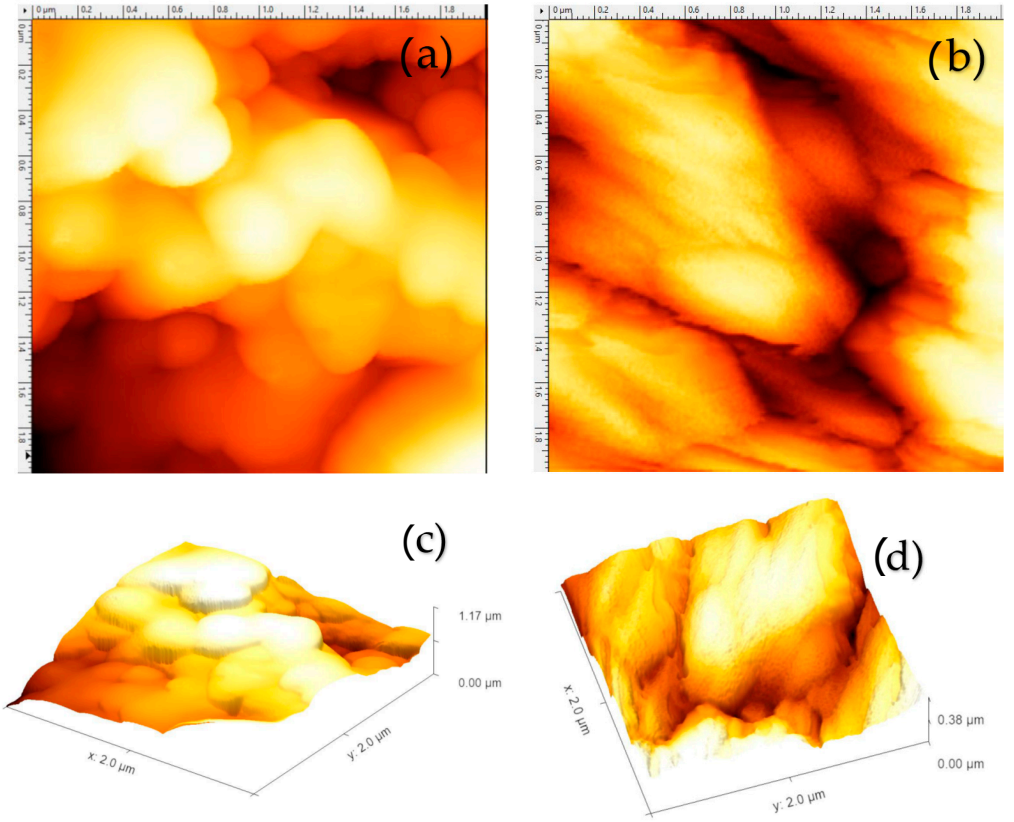

Figure 10. Porosity's surface changes as consequence of climate ageing: (**a**) before ageing; (**b**) after ageing. Topographic scan before (**c**) and after climate ageing (**d**).

In evaluating the 3D renderings, the Z scale is shown. While the original sample scan has an overall height difference of 1.17 microns, the aged sample scan shows an overall height difference of 0.38 microns. This observation is further supported by the

RMS roughness measurements (Figure 11), thus confirming that the deteriorated sample is far smoother (48.06 nm vs. 211.5 nm) when compared directly with the original undamaged coating.

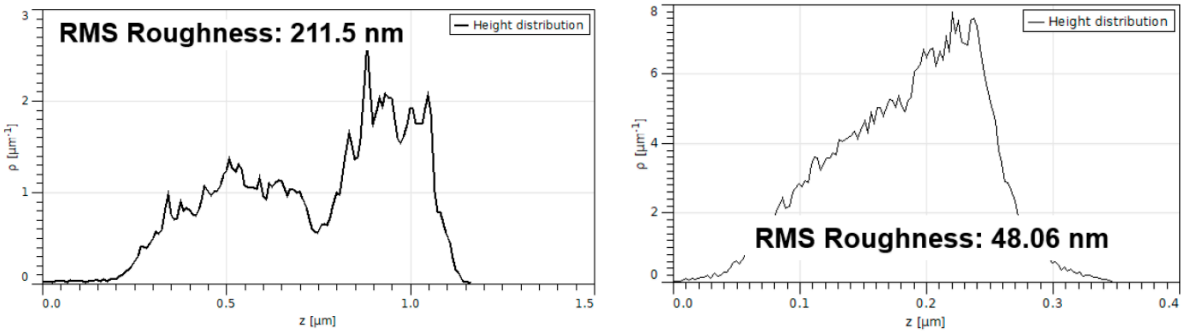

Figure 11. RMS roughness measurements: (**left**), before ageing; (**right**), after ageing.

Close phase examination evidenced the actual intercalation of both SPHB components and photocatalytically active nanoparticle phases. When comparing the differences between the phase images of the two samples (Figure 12), it is evident that the original undamaged coating has more contrast between the different phase zones. It is clear that the overall composition of the surfaces of undamaged and damaged samples is simply different, and this finding is ascribable to the loss of active BiZn nanoparticles due to the ageing process.

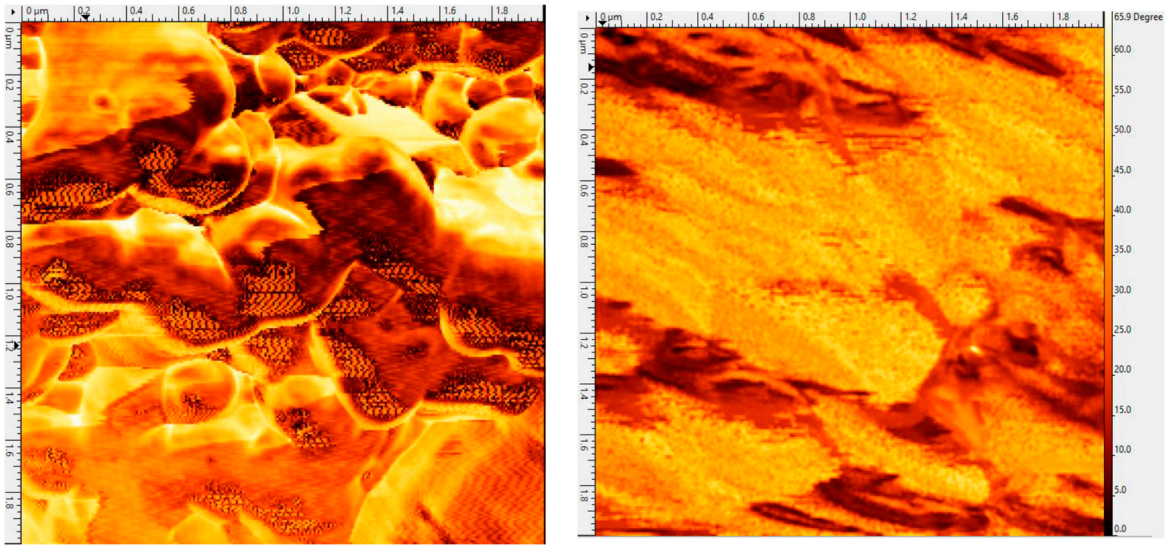

Figure 12. Phase images before (**left**) and after (**right**) the climate ageing.

NO_x degradation ability of coatings on substrates was also studied after subjecting them to climatic ageing. Results are collected in Figure 13.

It can be observed that the photocatalytic ability of the coatings to abate NO under solar light exposure dropped after ageing, showing an average reduction of ca. 36% for SPHB coatings and 41% for OHB coatings. This indicates that the harsh climatic conditions led to a significant decrease in photocatalytic activity due to the leaching and wash-out of the coatings. Interestingly, the limestone substrates retained substantial NO and NO_x removal rates. This finding aligns with the mineralogical composition of the substrate and its ability to adsorb nitrogen oxides, thereby enhancing their photocatalytic oxidation.

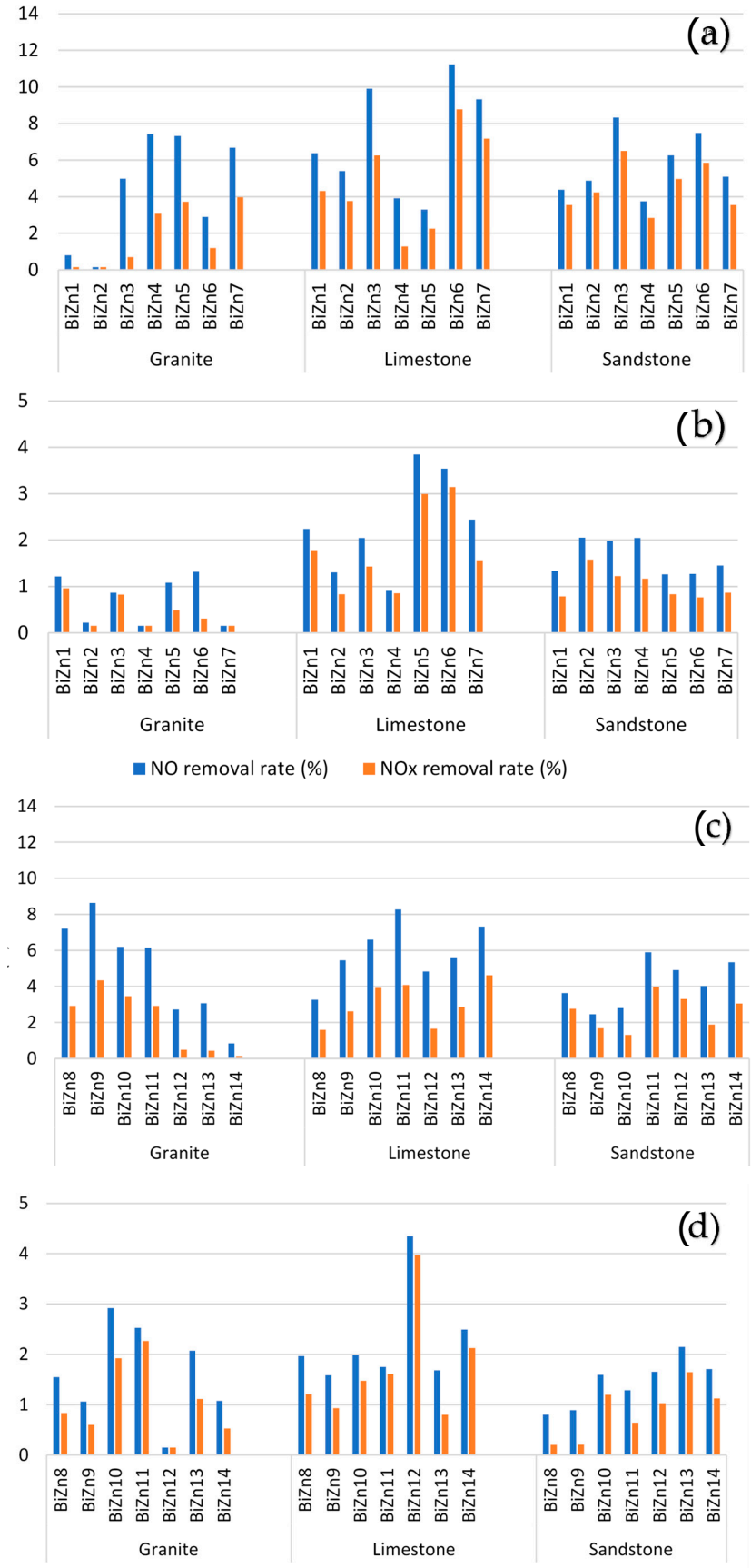

Figure 13. Photocatalytic NO and NO_x removal rates after climatic ageing of the SPHB coatings under (**a**) solar and (**b**) visible irradiation and OHB coatings under (**c**) solar and (**d**) visible irradiation.

A further study was devoted to examining colour stability in the coatings following climatic ageing. Findings showed that, despite the effects of climatic degradation, the coatings effectively prevented staining from dye deposition and simultaneously broke down the dye through photocatalytic oxidation. This dual action was attributed to the repellent properties of the hydrophobic matrices and the photocatalytic capabilities of the BiZn nanoparticles.

On average, SPHB coatings exhibited a self-cleaning capacity, resulting in a 40.3% reduction in the deposited dye over a period of 310 min. Conversely, OHB coatings led to a 55.4% discolouration.

3. Materials and Methods

3.1. Materials

The catalyst consists of nanoparticles of the heterostructures Bi_2O_3-ZnO (8 wt%/92 wt%), synthesized by Flame Spray Pyrolysis at the LUrederra Technological Centre. Organometallic precursors (ethyl hexanoates, acetylacetonates, butoxides, and propoxides) were used. The solvents used include isopropyl alcohol, toluene, xylene, and acetic acid. The precursor mixture included both the precursor for Bi and the precursor for Zn as well as appropriate solvents. The equipment used was based on Liquid-Feed Flame Spray Pyrolysis (LFFSP) technology, where a liquid precursor mixture is combined with a dispersing gas to generate droplets in a flame. The nanometric droplets, after solvent evaporation and nucleation, result in solid nanoparticles of the desired composition. A carrier gas is in charge of the transport and cooling of the generated nanoparticles from the pyrolysis area to specific filter bags where the nanopowder is retained. Precursor flows were in the range of 5–10 mL min^{-1}, and dispersion gas was between 10 and 30 L min^{-1}. The nozzle pressure was typically around 1–3 bar. With the aim of removing any trace of non-desirable adsorbed compounds, residual from the synthesis of the active agents, nanoparticles were calcined at 450 °C prior to their use.

Two media were used to vehicle the nanoparticles of the photocatalyst, one exhibiting superhydrophobic properties (SPHB) and the other with a hydro-oleophobic ability (OHB). The SPHB and OHB matrices are formed by three-dimensional (3D) structures of inorganic ceramic nano-oxides. The SPHB-specific formulation is commercially available in the market as TECNADIS AQUASHIELD FORTE. Its data sheet describes it as a see-through and low-viscosity fluid. This liquid incorporates ceramic nanooxides that confer hydrophobic properties. After application, the isopropanol evaporates, resulting in a formulation that is compatible with any porous construction material of interest. Additionally, this formulation contains stabilizing additives that prevent nanoparticle agglomeration and form a lightweight matrix through partial bonding with the ceramic nanooxides. This leads to the creation of a 3D structure that ensures the breathability of the porous substrate.

Similarly, there is another 3D formulation available at TECNAN, known as TECNADIS PRS PERFORMANCE. This formulation achieves a hydro-oleophobic effect. Its technical documentation characterizes it as a translucent and colourless liquid containing ceramic nanoparticles that confer water-repellent properties. These nanoparticles are dispersed within an organic medium, specifically 2-propanol, ensuring their compatibility with porous or slightly porous substrates commonly found in the construction industry.

The chosen porous substrates for study purposes included limestone, sandstone, and granite. DICONA S.A., the supplying company, was responsible for overseeing the extraction and cutting processes of these substrates. The cutting and processing procedures resulted in varying surface characteristics among the samples. Consequently, the primary surface features observed were a high degree of roughness in the sandstones, a moderate level of roughness in the limestones, and a smooth surface in the granites [35].

Utilizing X-ray diffraction analysis, it is possible to semi-quantitatively determine the mineralogical composition of these substrates. The limestone was sourced from Marbella, located in Málaga, Spain, and was composed of 99.5% calcite and 0.5% quartz. The sandstone originated from Lérida, Spain, and consisted of 39% calcite, 41% dolomite, and

20% quartz. The granite was procured from Porriño, Spain, and comprised 28% quartz, 53% alkaline feldspar (comprising 11% albite, 22% andesine, and 20% microcline), 6.5% pyroxene, 0.5% zirconium oxide, and 12% biotite and muscovite.

In terms of density, the values were as follows: 2.670 g/cm^3 for limestone, 2.302 g/cm^3 for sandstone, and 2.721 g/cm^3 for granite. The open porosity, which refers to the porosity accessible to water and is measured using a hydrostatic balance, exhibited the following values: 6.62% for limestone, 15.54% for sandstone, and 1.24% for granite. Total porosity values, determined through mercury intrusion porosimetry (MIP) [73], were as follows: 8.61% for limestone, 20.85% for sandstone, and 1.69% for granite. The stone supports have a prismatic shape, and their dimensions are 5x5x2 cm. Three different non-ionic dispersing agents were used: Tween20 (supplied by Panreac), Brij 35, and TritonX-100 (supplied by Sigma).

3.2. Methods

3.2.1. Characterization of Nanoparticles

The nanoparticles of Bi_2O_3-ZnO (8/92) were characterized, and the average diameter of the particles were determined by the physisorption of N_2 (Micromeritics ASAP 2020, Norcross, GA, USA) according to the BET algorithm. X-ray Fluorescence (XRF) measurements were accomplished with a Philips Magix Pro, PW2400.

To assess the photocatalytic effectiveness of the nanoparticles, a NO_x reduction test was conducted in a laminar flow reactor, as outlined in ISO 2016 standards [74]. This evaluation was carried out under two different lighting conditions: strictly visible radiation (with the use of a coloured glass filter (FGL420, Thorlabs, Newton, NJ, USA), which completely cuts off wavelengths shorter than 410 nm) and UV-VIS illumination. A 300 W Osram Ultravitalux lamp was used as the light source [75]. The lamp's nominal irradiance at a distance of 0.5 m after 1 h was measured to be 41.4 Wm^{-2} (780–400 nm), 13.6 Wm^{-2} (400–315 nm), and 3.0 Wm^{-2} (315–280 nm). This lamp emits a combination of visible, UVA, and UVB radiation, providing a credible simulation of solar light [76,77].

Initially, a concentration of 500 ppb of NO was introduced into the reactor at a flow rate of 3.0 L min^{-1}. To ensure that there is no adsorption on the samples, the system was kept in the dark for a period of 10 min. Subsequently, the lighting was activated, and the concentrations of both NO and NO_2 were monitored using a chemiluminescence detector (Environnement AC32M, Geneva, IL, USA). The samples were exposed to this illumination for 1 h, and once the lighting was turned off, the system was allowed to stand until the initial NO levels (500 ppb) were regained. Each experimental measurement was conducted in triplicate. The abatement efficiencies were determined by comparing the averages of the initial ten measurements (taken during the lamp's stabilization) with the averages of the final ten measurements (prior to turning off the lamp).

3.2.2. Preparation of Multifunctional Active Coatings and Evaluation of Their Efficiency

The compatibility and efficiency of the nanoparticles with the 3D structure were evaluated. In Table 5, the composition of the different coatings is displayed. The dispersions summarized in Table 5 were submitted to magnetic stirring for 45 min, and then they were applied to the stone support (5 × 5 × 2 cm) of granite, limestone, and sandstone. Each stone was kept in a horizontal position and was covered with 1 mL of solution. Stone samples were allowed to rest for 24 h, after which time they were completely dried.

Zeta potential studies were carried out to ascertain the stability of the suspensions, and titrations were conducted to check the effect of the addition of the dispersant on the catalyst by means of ZetaProbe Analyzer Colloidal Dynamics (Ponte Vedra Beach, FL, USA). BiZn 1% solutions (0.5 g of catalyst and 50 mL of solvent) and 0.1% dispersant solutions (0.1 g dispersant and 100 mL of solvent) were prepared for the titrations. The particle size distributions of the coatings were characterized by a size test with a laser diffractometer (Malvern Mastersizer, Malvern, United Kingdom).

Table 5. Composition of the different coatings.

SPHB Medium				
Coating	**Dispersant**	**Photocatalyst (g)**	**Dispersant (mg)**	**SPHB (mL)**
BiZn1	-	0.4	0	40
BiZn2	Tween20	0.4	3	40
BiZn3	Tween20	0.4	9	40
BiZn4	TritonX-100	0.4	3	40
BiZn5	TritonX-100	0.4	9	40
BiZn6	Brij35	0.4	3	40
BiZn7	Brij35	0.4	9	40
OHB Medium				
Coating	**Dispersant**	**Photocatalyst (g)**	**Dispersant (mg)**	**OHB (mL)**
BiZn8	-	0.4	0	40
BiZn9	Tween20	0.4	3	40
BiZn10	Tween20	0.4	9	40
BiZn11	TritonX-100	0.4	3	40
BiZn12	TritonX-100	0.4	9	40
BiZn13	Brij35	0.4	3	40
BiZn14	Brij35	0.4	9	40

The thicknesses of the coating layers were determined by a PosiTector 200 Ultrasonic Coating Thickness Gage, using an ultrasonic couplant gel supplied by Neurtek, Eibar, Spain.

To assess hydrophobicity and oleophobicity, static contact angle measurements and Advance and Receding Contact Angle (ARCA) tests were conducted using the OCA 15EC Dataphysics instrument from Filderstadt, Germany. For these experiments, 5 µL drops of water and hexadecane were, respectively, employed. Five different measurements were taken on each surface, and the reported results represent the averages. The contact angle was monitored for a duration of 10 s to ensure the reliability of the data, as detailed in a previous study [78].

It is worth noting that the contact angle assumes an idealized scenario where the surface is perfectly smooth and homogeneous. In reality, stone surfaces are often not completely smooth or uniform, resulting in significant variations in contact angle measurements across different points on the same surface. To address this issue, the ARCA (Advance and Receding Contact Angle) system is commonly employed. ARCA considers the presence of surface cavities. When liquids come into contact with these cavities, two extreme situations can occur:

- If the liquid fully penetrates the cavities, it is referred to as a Wenzel situation.
- If the liquid cannot expel the air trapped within the cavities, it is termed a Cassie–Baxter situation.

Both situations are thoroughly described in the literature [79].

Once the liquid drop makes initial contact with the surface of interest, injecting additional liquid compels it to fill the surface cavities, transitioning into what is known as the Wenzel state. Subsequently, by withdrawing some of the fluid, the drop is coerced into exiting the cavities, thus entering the Cassie–Baxter state. This shift between states affects the volume of the drop and, consequently, the contact angle, with an increase in volume corresponding to an advance angle in the Wenzel state and a decrease in volume leading to a receding angle in the Cassie–Baxter state. The difference between the advancing and receding angle values is termed hysteresis. Note that the force required to move a drop across a surface is inversely proportional to the hysteresis value. Studies have demonstrated that altering some aspects of the spherical drop's structure is necessary to move it on the surface [80].

A surface is considered super water-repellent when it exhibits a contact angle greater than 150 degrees and hysteresis of less than 10 degrees. In such cases, the force required to displace the drop on the surface is exceptionally low, indicating high repellency. Superhydrophobic surfaces typically possess rough textures, and their chemical composition can reduce surface free energy, enabling them to effectively repel water. As a result, surfaces with rougher coatings [81,82] and lower surface free energy [82] tend to have smaller surface-to-surface contact areas and exhibit less affinity for the liquid drop.

The photocatalytic activity of the coatings was assessed by means of an abatement test made in a laminar flow reactor (ISO 2016) to measure NO_x reduction with a 300 W Osram Ultravitalux lamp, according to the conditions detailed above in Section 3.2.1.

3.2.3. Durability of the Coatings after Accelerated Climatic Ageing

To assess the long-term performance of the coatings, a simulation of various climatic conditions was conducted within the FCH-XENOLAB 1500 climatic chamber (CCI, Barcelona, Spain). These simulation cycles incorporated alterations in temperature, exposure to UV-VIS radiation, variations in relative humidity, and exposure to artificial rainwater. Each cycle consisted of four 1 h phases, repeated six times, as follows:

- Maintaining conditions at 35 °C, with exposure to UV-VIS radiation and a relative humidity of 40%;
- Reducing temperature to 20 °C with a relative humidity of 90%, simulating rainwater exposure;
- Lowering the temperature further to 0 °C with a relative humidity of 60%;
- Extending the simulation to −5 °C with a relative humidity of 50%.

After accelerated weathering, the persistence of the photocatalytic ability was monitored by measuring the continuous NO_x abatement (according to the aforementioned method) as well as by colour degradation studies (self-cleaning performance).

In the samples showing the best performances, Atomic Force Microscopy (AFM) analysis was used to evaluate the changes in roughness and composition as a consequence of climatic ageing. A SA-AFM instrument (AFM Workshop, Hilton Head Island, SC, USA) and a 50-micron XY Scanner with a 17-micron Z range were required. The SA-AFM was calibrated with a 10 µm pitch reference standard from Bugdet Sensors with a 103 nm step height, HS-100MG. Calibrations affected the X, Y, and Z axes.

To evaluate the self-cleaning properties of the coatings, a colour degradation test was conducted using a 300 W Osram Ultravitalux lamp and a Konika Minolta spectrophotometer (Spectrophotometer CM-2300d, Tokyo, Japan). This test involved applying three layers of a 1mM solution of rhodamine B to the surface of the stone support using a brush. Subsequently, the samples were exposed to UV-VIS radiation at a distance of 20 cm from the radiation source. Data points were collected at intervals of 5, 20, 80, 140, and 310 min by measuring the coordinates L (luminosity), a (red-green range), and b (blue-yellow range). The degree of colour variation (ΔC_n) can be estimated through Equation (1).

$$\Delta C_n = \sqrt{\frac{\left[a_t^* - a_0^*\right]^2 + \left[b_t^* - b_0^*\right]^2}{\left[a_c^* - a_0^*\right]^2 + \left[b_c^* - b_0^*\right]^2}} \quad (1)$$

Equation (1): colour variation equation. Where a_t^* and b_t^* are coordinates at a given time, a_c^* and b_c^* are coordinates of undyed stones, and a_0^* and b_0^* are coordinates of newly dyed stones, as published in the article by Fornasini et al. [83].

The whole experimental procedure's scheme is shown in Figure 14.

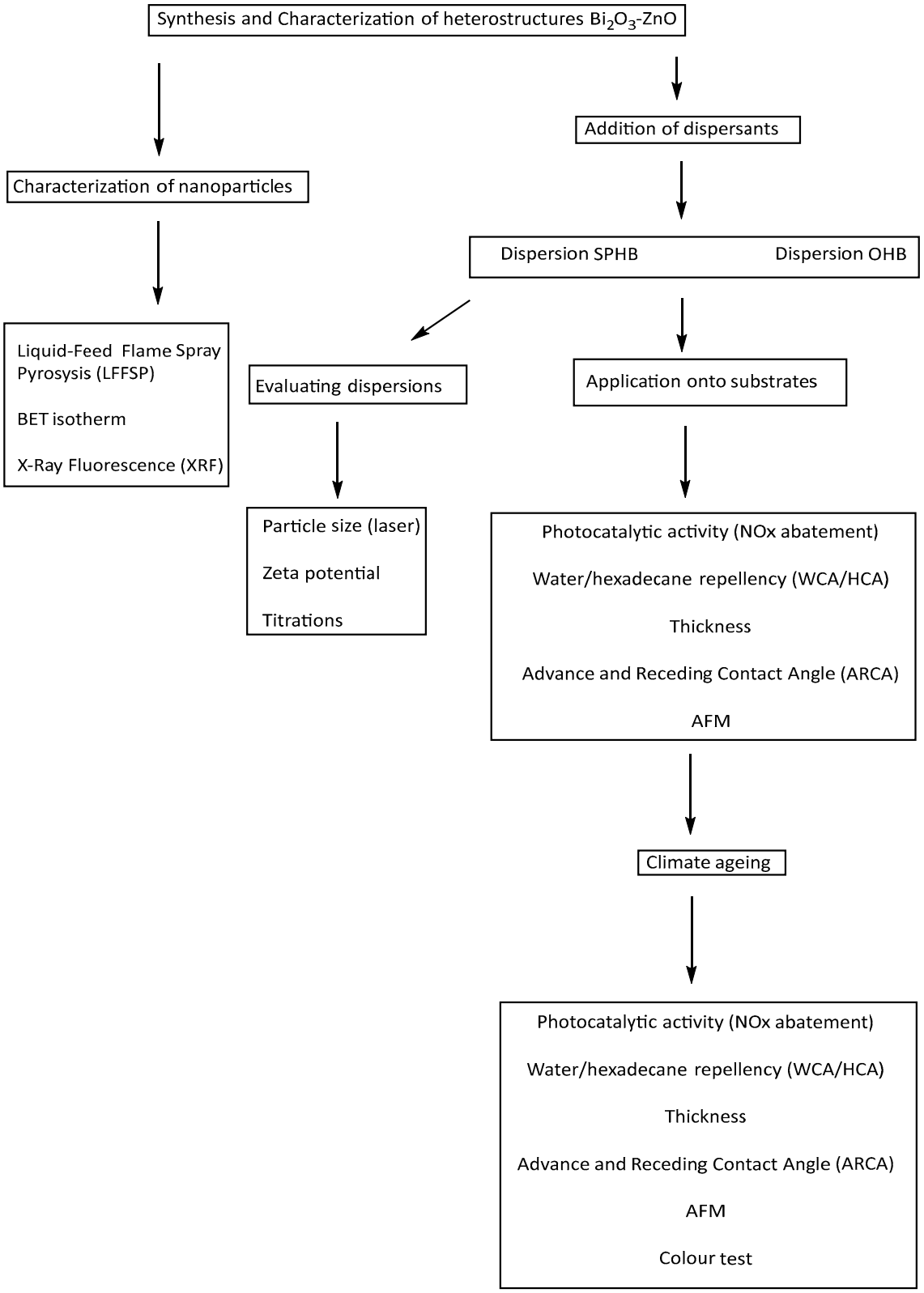

Figure 14. Scheme of the experimental work.

4. Conclusions

A combination of either superhydrophobic 3D inorganic structures (referred to as SPHB medium) or hydro-oleophobic 3D inorganic structures (referred to as OHB medium) and photocatalytic nanoparticles comprising heterostructures of Bi_2O_3-ZnO (8 wt%/92 wt%)

were used to create multifunctional coatings. These coatings were applied onto inorganic substrates commonly found in Built Heritage, namely granite, sandstone, and limestone. To prevent nanoparticle agglomeration, three non-ionic dispersants (Tween20, TritonX-100, and Brij35) were introduced in the coatings as well. It was observed that the use of dispersant agents led to an improvement in the dispersion's particle size distribution and enhanced photocatalytic efficiency. Among these, Brij-35, at its highest concentration (3%), revealed the most effective dispersing action, attributed to steric hindrance.

The applied coatings exhibited evident hydrophobic properties and, particularly in the case of OHB, showed a certain degree of oleophobic behaviour, too. The assessment of the coatings' static angles was influenced by the substrate's properties, with sandstone (possessing greater surface roughness) yielding the highest contact angles. In some cases, water contact angles exceeding 150° were recorded, indicating the superhydrophobic nature of these surfaces. The coatings displayed notable photocatalytic activity, especially when exposed to UV-VIS irradiation. According to the standard UNE 127197-1:2013, the SPHB coatings on limestone fell within Class 1 (NO_x removal between 4.0 and 6.0%), while those on sandstone were classified as Class 2 (with a removal range of 6.0–8.0%).

In SPHB coatings, Brij-35 emerged as the dispersant that most effectively enhanced photocatalytic efficiency, while in OHB coatings, Tween20 proved to be the most efficient dispersant, in agreement with particle size distribution measurements. OHB coatings, however, exhibited lower NO_x reductions compared with those observed in SPHB dispersions due to the shielding effect of the photocatalytic nanoparticles within the matrix.

Limestone substrates exhibited the highest photocatalytic removal of nitrogen oxides, attributed to the superior adsorption of NO and NO_x, as well as their subsequent photocatalytic degradation. This was enabled by the composition of the substrate, which was rich in alkaline-earth metal oxides and carbonates.

Accelerated climatic ageing studies conducted on treated specimens revealed a reduction in static contact angles and coating thickness. Despite this, SPHB coatings maintained their hydrophobicity. Atomic Force Microscopy (AFM) studies indicated the leaching of active nanoparticles and the washout of the coating. The photocatalytic activity also experienced a decrease (averaging 36% for the SPHB coatings). Even after undergoing severe accelerated climatic deterioration, the limestone substrates exhibited the most substantial rates of NO and NO_x removal, underscoring the effectiveness of these coatings in preventing water access and serving as photocatalytic surfaces. No adverse impacts were noted on the treated materials, affirming the safety of employing these coatings on Architectural Heritage.

Author Contributions: Conceptualization, J.I.Á., Í.N.-B., J.M.F. and V.M.T.-S.; methodology, V.M.T.-S., Í.N.-B., J.I.Á. and T.O.-M.; validation, V.M.T.-S. and C.F.-A.; formal analysis, V.M.T.-S. and Í.N.-B.; investigation, V.M.T.-S., T.O.-M., Í.N.-B. and J.I.Á.; resources, C.F.-A. and T.O.-M.; data curation, V.M.T.-S. and Í.N.-B.; writing—original draft preparation, V.M.T.-S.; writing—review and editing, J.M.F. and J.I.Á.; visualization, V.M.T.-S. and J.I.Á.; supervision, J.I.Á. and Í.N.-B.; project administration, J.I.Á. and Í.N.-B.; funding acquisition, J.I.Á. and Í.N.-B. All authors have read and agreed to the published version of the manuscript.

Funding: Funded by the Spanish Ministerio de Ciencia e Innovación MICINN, grants numbers PID2020-119975RB-100 LIMORTHER, Terra Cycle TED2021-129705-C33 grant, and by Government of Navarra, PC142-143 MULTIFICON. Thanks are given to the Programa de Ayudas Adscritas a Proyectos de la Universidad de Navarra for a predoctoral grant.

Data Availability Statement: The data presented in this study are available upon request from the corresponding author. The data are not publicly available due to privacy concerning regard the results, which are industrial secrets.

Acknowledgments: The authors would like to thank MTB Spain for the help with the AFM measurements.

Conflicts of Interest: The authors declare no conflict of interest. The funders had no role in the design of the study; in the collection, analyses, or interpretation of data; in the writing of the manuscript; or in the decision to publish the results.

References

1. Brimblecombe, P.; Grossi, C.M. Aesthetic thresholds and blackening of stone buildings. *Sci. Total Environ.* **2005**, *349*, 175–189. [CrossRef] [PubMed]
2. Gulotta, D.; Villa, F.; Cappitelli, F.; Toniolo, L. Biofilm colonization of metamorphic lithotypes of a renaissance cathedral exposed to urban atmosphere. *Sci. Total Environ.* **2018**, *639*, 1480–1490. [CrossRef] [PubMed]
3. Pozo-Antonio, J.S.; Puente, I.; Pereira, M.F.C.; Rocha, C.S.A. Quantification and mapping of deterioration patterns on granite surfaces by means of mobile LiDAR data. *Measurement* **2019**, *140*, 227–236. [CrossRef]
4. Vidal, F.; Vicente, R.; Mendes Silva, J. Review of environmental and air pollution impacts on built heritage: 10 questions on corrosion and soiling effects for urban intervention. *J. Cult. Herit.* **2019**, *37*, 273–295. [CrossRef]
5. Brai, M.; Camaiti, M.; Casieri, C.; De Luca, F.; Fantazzini, P. Nuclear magnetic resonance for cultural heritage. *Magn. Reson. Imaging* **2007**, *25*, 461–465. [CrossRef]
6. Piuzzi, E.; Pittella, E.; Pisa, S.; Cataldo, A.; De Benedetto, E.; Cannazza, G. An improved noninvasive resonance method for water content characterization of Cultural Heritage stone materials. *Measurement* **2018**, *125*, 257–261. [CrossRef]
7. Gomes, V.; Dionísio, A.; Pozo-Antonio, J.S.; Rivas, T.; Ramil, A. Mechanical and laser cleaning of spray graffiti paints on a granite subjected to a SO_2-rich atmosphere. *Constr. Build. Mater.* **2018**, *188*, 621–632. [CrossRef]
8. Sanmartín, P.; Cappitelli, F.; Mitchell, R. Current methods of graffiti removal: A review. *Constr. Build. Mater.* **2014**, *71*, 363–374. [CrossRef]
9. Fermo, P.; Cappelletti, G.; Cozzi, N.; Padeletti, G.; Kaciulis, S.; Brucale, M.; Merlini, M. Hydrophobizing coatings for cultural heritage. A detailed study of resin/stone surface interaction. *Appl. Phys. A* **2014**, *116*, 341–348. [CrossRef]
10. Manoudis, P.N.; Tsakalof, A.; Karapanagiotis, I.; Zuburtikudis, I.; Panayiotou, C. Fabrication of super-hydrophobic surfaces for enhanced stone protection. *Surf. Coat. Technol.* **2009**, *203*, 1322–1328. [CrossRef]
11. Toniolo, L.; Poli, T.; Castelvetro, V.; Manariti, A.; Chiantore, O.; Lazzari, M. Tailoring new fluorinated acrylic copolymers as protective coatings for marble. *J. Cult. Herit.* **2002**, *3*, 309–316. [CrossRef]
12. Alessandrini, G.; Aglietto, M.; Castelvetro, V.; Ciardelli, F.; Peruzzi, R.; Toniolo, L. Comparative evaluation of fluorinated and unfluorinated acrylic copolymers as water-repellent coating materials for stone. *J. Appl. Polym. Sci.* **2000**, *76*, 962–977. [CrossRef]
13. Andreotti, S.; Franzoni, E.; Fabbri, P. Poly(hydroxyalkanoate)s-Based Hydrophobic Coatings for the Protection of Stone in Cultural Heritage. *Materials* **2018**, *11*, 165. [CrossRef]
14. Aslanidou, D.; Karapanagiotis, I.; Lampakis, D. Waterborne Superhydrophobic and Superoleophobic Coatings for the Protection of Marble and Sandstone. *Materials* **2018**, *11*, 585. [CrossRef]
15. Winandy, L.; Schlebusch, O.; Fischer, R. Fungal hydrophobins render stones impermeable for water but keep them permeable for vapor. *Sci. Rep.* **2019**, *9*, 6264. [CrossRef]
16. Macchia, A.; Ruffolo, S.A.; Rivaroli, L.; Malagodi, M.; Licchelli, M.; Rovella, N.; Randazzo, L.; La Russa, M.F. Comparative study of protective coatings for the conservation of Urban Art. *J. Cult. Herit.* **2020**, *41*, 232–237. [CrossRef]
17. Turk, J.; Mauko Pranjić, A.; Hursthouse, A.; Turner, R.; Hughes, J.J. Decision support criteria and the development of a decision support tool for the selection of conservation materials for the built cultural heritage. *J. Cult. Herit.* **2019**, *37*, 44–53. [CrossRef]
18. Liu, Q.; Zhang, B.J. Syntheses of a novel nanomaterial for conservation of historic stones inspired by nature. *Mater. Lett.* **2007**, *61*, 4976–4979. [CrossRef]
19. Melo, M.J.; Bracci, S.; Camaiti, M.; Chiantore, O.; Piacenti, F. Photodegradation of acrylic resins used in the conservation of stone. *Polym. Degrad. Stabil.* **1999**, *66*, 23–30. [CrossRef]
20. Doehne, E.F.; Price, C.A. *Stone Conservation: An Overview of Current Research*, 2nd ed.; Getty Conservation Institute: Los Angeles, CA, USA, 2010; p. 158.
21. Bergamonti, L.; Alfieri, I.; Lorenzi, A.; Predieri, G.; Barone, G.; Gemelli, G.; Mazzoleni, P.; Raneri, S.; Bersani, D.; Lottici, P.P. Nanocrystalline TiO_2 coatings by sol–gel: Photocatalytic activity on Pietra di Noto biocalcarenite. *J. Sol-Gel Sci. Technol.* **2015**, *75*, 141–151. [CrossRef]
22. Kapridaki, C.; Maravelaki-Kalaitzaki, P. TiO_2–SiO_2–PDMS nano-composite hydrophobic coating with self-cleaning properties for marble protection. *Prog. Org. Coat.* **2013**, *76*, 400–410. [CrossRef]
23. Kapridaki, C.; Pinho, L.; Mosquera, M.J.; Maravelaki-Kalaitzaki, P. Producing photoactive, transparent and hydrophobic SiO_2-crystalline TiO_2 nanocomposites at ambient conditions with application as self-cleaning coatings. *Appl. Catal. B Environ.* **2014**, *156–157*, 416–427. [CrossRef]
24. Licciulli, A.; Calia, A.; Lettieri, M.; Diso, D.; Masieri, M.; Franza, S.; Amadelli, R.; Casarano, G. Photocatalytic TiO_2 coatings on limestone. *J. Sol-Gel Sci. Technol.* **2011**, *60*, 437–444. [CrossRef]
25. Wolfrum, E.J.; Huang, J.; Blake, D.M.; Maness, P.-C.; Huang, Z.; Fiest, J.; Jacoby, W.A. Photocatalytic Oxidation of Bacteria, Bacterial and Fungal Spores, and Model Biofilm Components to Carbon Dioxide on Titanium Dioxide-Coated Surfaces. *Environ. Sci. Technol.* **2002**, *36*, 3412–3419. [CrossRef] [PubMed]
26. Ghosh, S.; Patra, R.; Majumdar, D.; Sen, K. Developing scenario of titania-based building materials for environmental remediation. *Int. J. Environ. Sci. Technol.* **2021**, *18*, 2077–2102. [CrossRef]
27. Russell, H.S.; Frederickson, L.B.; Hertel, O.; Ellermann, T.; Jensen, S.S. A Review of Photocatalytic Materials for Urban NO_x Remediation. *Catalysts* **2021**, *11*, 675. [CrossRef]

28. Folli, A.; Strøm, M.; Madsen, T.P.; Henriksen, T.; Lang, J.; Emenius, J.; Klevebrant, T.; Nilsson, A. Field study of air purifying paving elements containing TiO_2. *Atmos. Environ.* **2015**, *107*, 44–51. [CrossRef]
29. Yang, F.; Takahashi, Y.; Sakai, N.; Tatsuma, T. Visible light driven photocatalysts with oxidative energy storage abilities. *J. Mater. Chem.* **2011**, *21*, 2288–2293. [CrossRef]
30. Du, Q.; Ma, J.; Shao, X.; Wang, W.; Tian, G. Core-shell structured TiO_2@In_2O_3 for highly active visible-light photocatalysis. *Chem. Phys. Lett.* **2019**, *714*, 208–212. [CrossRef]
31. Mas, N.; Hueso, J.L.; Martinez, G.; Madrid, A.; Mallada, R.; Ortega-Liebana, M.C.; Bueno-Alejo, C.; Santamaria, J. Laser-driven direct synthesis of carbon nanodots and application as sensitizers for visible-light photocatalysis. *Carbon* **2020**, *156*, 453–462. [CrossRef]
32. Zhao, J.; Dang, Z.; Muddassir, M.; Raza, S.; Zhong, A.; Wang, X.; Jin, J. A New Cd(II)-Based Coordination Polymer for Efficient Photocatalytic Removal of Organic Dyes. *Molecules* **2023**, *28*, 6848. [CrossRef]
33. Jin, J.; Wang, J.; Guo, J.; Yan, M.-H.; Wang, J.; Srivastava, D.; Kumar, A.; Sakiyama, H.; Muddassir, M.; Pan, Y. A 3D rare cubane-like tetramer Cu(II)-based MOF with 4-fold dia topology as an efficient photocatalyst for dye degradation. *Colloids Surf. A Physicochem. Eng. Asp.* **2023**, *656*, 130475. [CrossRef]
34. Pérez-Nicolás, M.; Plank, J.; Ruiz-Izuriaga, D.; Navarro-Blasco, I.; Fernández, J.M.; Alvarez, J.I. Photocatalytically active coatings for cement and air lime mortars: Enhancement of the activity by incorporation of superplasticizers. *Constr. Build. Mater.* **2018**, *162*, 628–648. [CrossRef]
35. Speziale, A.; González-Sánchez, J.F.; Taşcı, B.; Pastor, A.; Sánchez, L.; Fernández-Acevedo, C.; Oroz-Mateo, T.; Salazar, C.; Navarro-Blasco, I.; Fernández, J.M.; et al. Development of Multifunctional Coatings for Protecting Stones and Lime Mortars of the Architectural Heritage. *Int. J. Archit. Herit.* **2020**, *14*, 1008–1029. [CrossRef]
36. Zhao, L.; Xia, M.; Liu, Y.; Zheng, B.; Jiang, Q.; Lian, J. Structure and Photocatalysis of TiO_2/ZnO Double-Layer Film Prepared by Pulsed Laser Deposition. *Mater. Trans.* **2012**, *53*, 463–468. [CrossRef]
37. Reverberi, A.P.; Varbanov, P.S.; Vocciante, M.; Fabiano, B. Bismuth oxide-related photocatalysts in green nanotechnology: A critical analysis. *Front. Chem. Sci. Eng.* **2018**, *12*, 878–892. [CrossRef]
38. Rani, M.; Keshu Shanker, U. Efficient degradation of organic pollutants by novel titanium dioxide coupled bismuth oxide nanocomposite: Green synthesis, kinetics and photoactivity. *J. Environ. Manag.* **2021**, *300*, 113777. [CrossRef] [PubMed]
39. Hwang, Y.C.; Lee, S.H.; Hwang, I.N.; Kang, I.C.; Kim, M.S.; Kim, S.H.; Son, H.H.; Oh, W.M. Chemical composition, radiopacity, and biocompatibility of Portland cement with bismuth oxide. *Oral Surg. Oral Med. Oral Pathol. Oral Radiol. Endod.* **2009**, *107*, e96–e102. [CrossRef] [PubMed]
40. Shajari-Ghasemkheili, S.; Sarraf-Mamoory, R. Development of a transparent silica-titania-methyl siliconate nanocoating with photocatalytic-hydrophobic properties aided by response surface method. *Mater. Res. Express.* **2019**, *6*, 106430. [CrossRef]
41. Aldoasri, M.A.; Darwish, S.S.; Adam, M.A.; Elmarzugi, N.A.; Ahmed, S.M. Protecting of Marble Stone Facades of Historic Buildings Using Multifunctional TiO_2 Nanocoatings. *Sustainability* **2017**, *9*, 2002. [CrossRef]
42. Colangiuli, D.; Lettieri, M.; Masieri, M.; Calia, A. Field study in an urban environment of simultaneous self-cleaning and hydrophobic nanosized TiO_2-based coatings on stone for the protection of building surface. *Sci. Total Environ.* **2019**, *650*, 2919–2930. [CrossRef] [PubMed]
43. Gobakis, K.; Kolokotsa, D.; Maravelaki-Kalaitzaki, N.; Perdikatsis, V.; Santamouris, M. Development and analysis of advanced inorganic coatings for buildings and urban structures. *Energy Build.* **2015**, *89*, 196–205. [CrossRef]
44. Kamegawa, T.; Irikawa, K.; Yamashita, H. Unique Surface Properties of Nanocomposite Thin Film Photocatalysts of TiO_2 and Poly(tetrafluoroethylene). *Chem. Lett.* **2015**, *44*, 509–511. [CrossRef]
45. Kamegawa, T.; Shimizu, Y.; Yamashita, H. Superhydrophobic Surfaces with Photocatalytic Self-Cleaning Properties by Nanocomposite Coating of TiO_2 and Polytetrafluoroethylene. *Adv. Mater.* **2012**, *24*, 3697–3700. [CrossRef]
46. Kapridaki, C.; Maravelaki, N.P. *TiO_2–SiO_2–PDMS Nanocomposites with Self-Cleaning Properties for Stone Protection and Consolidation*; Geological Society, London, Special Publications: London, UK, 2016; Volume 416, pp. 285–292.
47. Lanka, S.; Alexandrova, E.; Kozhukhova, M.; Hasan, M.S.; Nosonovsky, M.; Sobolev, K. Tribological and Wetting Properties of TiO_2 Based Hydrophobic Coatings for Ceramics. *J. Tribol.* **2019**, *141*, 101301. [CrossRef]
48. La Russa, M.F.; Ruffolo, S.A.; Rovella, N.; Belfiore, C.M.; Palermo, A.M.; Guzzi, M.T.; Crisci, G.M. Multifunctional TiO_2 coatings for Cultural Heritage. *Prog. Org. Coat.* **2012**, *74*, 186–191. [CrossRef]
49. Lau, K.K.S.; Bico, J.; Teo, K.B.K.; Chhowalla, M.; Amaratunga, G.A.J.; Milne, W.I.; McKinley, G.H.; Gleason, K.K. Superhydrophobic Carbon Nanotube Forests. *Nano Lett.* **2003**, *3*, 1701–1705. [CrossRef]
50. Meseck, G.R.; Käch, A.; Seeger, S. Three-Dimensional Organization of Surface-Bound Silicone Nanofilaments Revealed by Focused Ion Beam Nanotomography. *J. Phys. Chem. C* **2014**, *118*, 24967–24975. [CrossRef]
51. Lee, C.G.; Na, K.H.; Kim, W.T.; Park, D.C.; Yang, W.H.; Choi, W.Y. TiO_2/ZnO Nanofibers Prepared by Electrospinning and Their Photocatalytic Degradation of Methylene Blue Compared with TiO_2 Nanofibers. *Appl. Sci.* **2019**, *9*, 3404. [CrossRef]
52. Liu, Y.; Cai, T.; Wang, L.; Zhang, S.; Zhang, G.; Xia, X. Hollow Microsphere TiO_2/ZnO p–n Heterojuction with High Photocatalytic Performance for 2,4-Dinitropheno Mineralization. *Nano* **2017**, *12*, 1750076. [CrossRef]
53. Low, J.; Yu, J.; Jaroniec, M.; Wageh, S.; Al-Ghamdi, A.A. Heterojunction Photocatalysts. *Adv. Mater.* **2017**, *29*, 1601694. [CrossRef]
54. Šutka, A.; Järvekülg, M.; Gross, K.A. Photocatalytic Nanoheterostructures and Chemically Bonded Junctions Made by Solution-Based Approaches. *Crit. Rev. Solid State Mat. Sci.* **2019**, *44*, 239–263. [CrossRef]

55. Thakur, S.; Maiti, S.; Pal, S.; Chattopadhyay, K.K. Geometrically Intricate Oxide-Based Heterostructure Over Flexible Platform: Morphology-Induced Catalytic Performance Enhancement Under UV Light. International Conference on Communication, Devices and Networking, ICCDN 2017. In *Advances in Communication, Devices and Networking: Proceedings of ICCDN 2017*; Sarkar, S.K., Bera, R., Chakraborty, S., Eds.; Springer: Berlin, Germany, 2018; pp. 21–27. [CrossRef]
56. Ungan, H.; Tekin, T. Effect of the sonication and coating time on the photocatalytic degradation of TiO_2, TiO_2-Ag, and TiO_2-ZnO thin film photocatalysts. *Chem. Eng. Commun.* **2020**, *207*, 896–903. [CrossRef]
57. Wang, H.; Zhang, L.; Chen, Z.; Hu, J.; Li, S.; Wang, Z.; Liu, J.; Wang, X. Semiconductor heterojunction photocatalysts: Design, construction, and photocatalytic performances. *Chem. Soc. Rev.* **2014**, *43*, 5234–5244. [CrossRef] [PubMed]
58. Duran, A.; González-Sánchez, J.F.; Fernández, J.M.; Sirera, R.; Navarro-Blasco, Í.; Alvarez, J.I. Influence of Two Polymer-Based Superplasticizers (Poly-naphthalene Sulfonate, PNS, and Lignosulfonate, LS) on Compressive and Flexural Strength, Freeze-Thaw, and Sulphate Attack Resistance of Lime-Metakaolin Grouts. *Polymers* **2018**, *10*, 824. [CrossRef] [PubMed]
59. Yang Teoh, W.; Amal, R.; Mädler, L. Flame spray pyrolysis: An enabling technology for nanoparticles design and fabrication. *Nanoscale* **2010**, *2*, 1324–1347. [CrossRef]
60. Plank, J.; Vlad, D.; Brandl, A.; Chatziagorastou, P. Colloidal chemistry examination of the steric effect of polycarboxylate superplasticizers. *Cem. Int.* **2005**, *3*, 100–110. [CrossRef]
61. Liu, X.; Chen, G.; Su, C. Effects of material properties on sedimentation and aggregation of titanium dioxide nanoparticles of anatase and rutile in the aqueous phase. *J. Colloid Interface Sci.* **2011**, *363*, 84–91. [CrossRef]
62. Kong, H.J.; Bike, S.G.; Li, V.C. Electrosteric stabilization of concentrated cement suspensions imparted by a strong anionic polyelectrolyte and a non-ionic polymer. *Cem. Concr. Res.* **2006**, *36*, 842–850. [CrossRef]
63. Hong, I.K.; Kim, S.I.; Lee, S.B. Effects of HLB value on oil-in-water emulsions: Droplet size, rheological behavior, zeta-potential, and creaming index. *J. Ind. Eng. Chem.* **2018**, *67*, 123–131. [CrossRef]
64. Liu, Q.; Chen, Z.; Yang, Y. Study of the Air-Entraining Behavior Based on the Interactions between Cement Particles and Selected Cationic, Anionic and Nonionic Surfactants. *Materials* **2020**, *13*, 3514. [CrossRef]
65. Tkachenko, N.H.; Yaremko, Z.M.; Bellmann, C.; Soltys, M.M. The influence of ionic and nonionic surfactants on aggregative stability and electrical surface properties of aqueous suspensions of titanium dioxide. *J. Colloid Interface Sci.* **2006**, *299*, 686–695. [CrossRef] [PubMed]
66. Rivera, M.; Edgar, M.; Melo, R. La rugosidad de las superficies: Topometría. *Ingenierías* **2001**, *4*, 27–33.
67. *UNE-EN 127197-1:2013*; Application of the Test Method to Evaluate the Performance in Air Purification Using Photocatalytic Semiconductor Materials Embedded in Precast Concrete Products. Part 1: Elimination of Nitrogen Oxides. UNE-EN (Una Norma Española-European Norm): Madrid, Spain, 2013.
68. Ballari, M.M.; Yu, Q.L.; Brouwers, H.J.H. Experimental study of the NO and NO_2 degradation by photocatalytically active concrete. *Catal. Today* **2011**, *1*, 175–180. [CrossRef]
69. Dylla, H.; Hassan, M.M.; Mohammad, L.N.; Rupnow, T.; Wright, E. Evaluation of environmental effectiveness of titanium dioxide photocatalyst coating for concrete pavement. *Trans. Res. Rec.* **2010**, *2164*, 46–51. [CrossRef]
70. Cros, C.J.; Terpeluk, A.L.; Crain, N.E.; Juenger, M.C.G.; Corsi, R.L. Influence of environmental factors on removal of oxides of nitrogen by a photocatalytic coating. *J. Air Waste Manag. Assoc.* **2015**, *65*, 937–947. [CrossRef] [PubMed]
71. Yasin, M.; Saeed, M.; Muneer, M.; Usman, M.; Haq, A.U.; Sadia, M.; Altaf, M. Development of Bi_2O_3-ZnO heterostructure for enhanced photodegradation of rhodamine B and reactive yellow dyes. *Surf. Interfaces* **2022**, *30*, 101846. [CrossRef]
72. Pérez-Nicolás, M.; Balbuena, J.; Cruz-Yusta, M.; Sánchez, L.; Navarro-Blasco, I.; Fernández, J.; Alvarez, J. Photocatalytic NO_x abatement by calcium aluminate cements modified with TiO_2: Improved NO_2 conversion. *Cem. Concr. Res.* **2015**, *70*, 67–76. [CrossRef]
73. Navarro-Blasco, Í.; Fernández, J.M.; Duran, A.; Sirera, R.; Álvarez, J.I. A novel use of calcium aluminate cements for recycling waste foundry sand (WFS). *Constr. Build. Mater.* **2013**, *48*, 218–228. [CrossRef]
74. *ISO 22197-1:2016*; Fine Ceramics (Advanced Ceramics, Advanced Technical Ceramics)—Test Method for Air Purification Performance of Semiconducting Photocatalytic Materials—Part 1: Removal of Nitric Oxide. ISO (International Organization for Standardization): Geneva, Switzerland, 2016.
75. Pérez-Nicolás, M.; Navarro-Blasco, I.; Fernández, J.M.; Alvarez, J.I. Atmospheric NO_x removal: Study of cement mortars with iron- and vanadium-doped TiO_2 as visible light–sensitive photocatalysts. *Constr. Build. Mater.* **2017**, *149*, 257–271. [CrossRef]
76. Heikkilä, U.; Beer, J.; Feichter, J. Meridional transport and deposition of atmospheric 10Be. *Atmos. Chem. Phys.* **2009**, *9*, 515–527. [CrossRef]
77. Prieto, C.; Lagaron, J.M. Nanodroplets of Docosahexaenoic Acid-Enriched Algae Oil Encapsulated within Microparticles of Hydrocolloids by Emulsion Electrospraying Assisted by Pressurized Gas. *Nanomaterials* **2020**, *10*, 270. [CrossRef] [PubMed]
78. Fronzi, M.; Assadi, M.H.N.; Hanaor, D.A.H. Theoretical insights into the hydrophobicity of low index CeO_2 surfaces. *Appl. Surf. Sci.* **2019**, *478*, 68–74. [CrossRef]
79. Han, S.; Yang, R.; Li, C.; Yang, L. The Wettability and Numerical Model of Different Silicon Microstructural Surfaces. *Appl. Sci.* **2019**, *9*, 566. [CrossRef]
80. Gao, L.; McCarthy, T.J. A Perfectly Hydrophobic Surface (θ A/θ R = 180°/180°). *J. Am. Chem. Soc.* **2006**, *128*, 9052–9053. [CrossRef]
81. Sbeih, S.; Steffen, W.; Kappl, M. Anti-wettability of Chemically and Physically Modified Glass Surfaces. *Adv. Mater. Proc.* **2021**, *6*, 21010421. [CrossRef]

82. González Sánchez, A. Obtención de Recubrimientos Superhidrofugantes Para Materiales de Construcción, Mediante el Uso de Nanopartículas de Sílice Funcionalizadas. Bachelor's Thesis, UCA, Cádiz, Spain, 2016. Available online: https://rodin.uca.es/handle/10498/20685 (accessed on 25 March 2023).
83. Fornasini, L.; Bergamonti, L.; Bondioli, F.; Bersani, D.; Lazzarini, L.; Paz, Y.; Lottici, P.P. Photocatalytic N-doped TiO_2 for self-cleaning of limestones. *Eur. Phys. J. Plus.* **2019**, *134*, 539. [CrossRef]